Journal of Sound and Vibration 608 (2025) 119077

Contents lists available at ScienceDirect

Journal of Sound and Vibration

journal homepage: www.elsevier.com/locate/jsvi

Controlling instability of high-speed magnetically suspended vehicles: The interaction of the electromagnetic and wave-induced instability mechanisms

Andrei B. Fărăgău *, Andrei V. Metrikine, Jithu Paul, Rens van Leijden, Karel N. van Dalen

Faculty of Civil Engineering and Geosciences, Delft University of Technology, Stevinweg 1, 2628 CN Delft, The Netherlands

ARTICLE INFO

Keywords:
Maglev
Hyperloop
Stability
Electromagnetic suspension
Hopf bifurcation
Limit cycle
Wave-induced instability
Anomalous doppler waves

ABSTRACT

Maglev and the newer Hyperloop technologies are advanced transportation systems that eliminate wheel–rail friction using electromagnetic suspension/levitation. The electromagnetic suspension is inherently unstable and requires a control strategy for safe operation, which has been previously studied in the context of Maglev. However, the interaction between electromagnetic instability and another instability mechanism, known as wave-induced instability, occurring at high vehicle velocities, has not been explored. This interaction between two distinct instability mechanisms is the focus of this study. From a practical perspective, this study examines the stability of magnetically suspended vehicles (e.g., Maglev or Hyperloop) in relation to vehicle velocity and control gains. To account for this, this study properly includes the infinite guideway, thus allowing vehicle velocity to influence system stability. The results show that at sub-critical velocities, the guideway's reaction force helps suppress perturbations and stabilize the system, with instability driven solely by improper electromagnetic control. However, at super-critical velocities, wave-induced instability drastically reduces the stable parameter space. This study further proposes a methodology to distinguish the contribution of each instability mechanism to the overall system stability, which is important for efficient mitigation measures. The findings reveal that beyond a certain super-critical velocity, wave-induced instability dominates much of the control-gain plane, with the control strategy effective in only limited regions. In conclusion, the study recommends revising control design strategies, as solely focusing on maximizing energy dissipation through control can trigger wave-induced instability. A more effective approach balances energy dissipation with avoiding the activation of wave-induced instability by steering clear of problematic vibration frequencies. These insights provide guidance for improving control strategies.

1. Introduction

Magnetically levitated (Maglev) vehicles and, more recently, Hyperloop are cutting-edge transportation technologies currently under development. Unlike traditional railways, these systems eliminate wheel–rail contact friction by employing electromagnetic suspension/levitation. Additionally, Hyperloop further reduces air resistance by operating within a de-pressurized tube. These

* Corresponding author.
E-mail address: A.B.Faragau@tudelft.nl (A.B. Fărăgău).

https://doi.org/10.1016/j.jsv.2025.119077
Received 15 October 2024; Received in revised form 19 March 2025; Accepted 20 March 2025
Available online 30 March 2025

advancements offer significant advantages over conventional railway systems: (i) substantial noise reduction by eliminating wheel–rail interaction and, in the case of Hyperloop, eliminating also aerodynamic noise; and (ii) notable energy savings by reducing friction losses from wheel–rail contact and aerodynamic drag, for Hyperloop specifically. Moreover, these innovative designs can potentially reach significantly higher speeds than traditional railways, making Maglev and Hyperloop promising environmentally friendly alternatives to air travel.

Numerous challenges confronting Maglev and Hyperloop systems have already been identified and investigated within the framework of high-speed railways, encompassing: vehicle–structure-soil interaction at high velocities [1–5], fatigue and deterioration at critical structural locations such as transition zones [6–9], the impact of guideway periodicity on system response [5,10], system stability concerns [11–13], among many others. Nevertheless, several novel challenges are expected to arise [14,15]. A significant obstacle to deploying Maglev and Hyperloop technologies is the substantial cost of constructing the guideway, which constitutes the most expensive component [16]. Thus, an efficient guideway design is essential to make these transportation systems more attractive. While a more flexible guideway is initially less expensive (excluding long-term fatigue issues), it can cause undesired vehicle–structure interactions. Next to optimizing guideway design, another solution could involve developing an efficient control system to minimize response amplification, even with a very flexible guideway. Therefore, a balance between constructing a rigid (and costly) guideway and designing intelligent vehicle control systems (which can be technologically difficult and energy intensive) must be considered to make Maglev and Hyperloop technologies economically viable [16].

The most cost-effective solution can be achieved by selecting the most flexible guideway for which the control system can ensure the dynamic stability of the vehicle-guideway interaction at high velocities, thereby preventing excessive response amplification. Even with a *rigid* guideway, dynamic instability in Maglev and Hyperloop transportation systems can still arise due to factors such as: improper control of the electromagnetic suspension (EMS) system [17,18], inadequate design of the electrodynamic system (EDS) [19–21], significant time delays in the control system [22], aerodynamic instability (e.g., flutter [18,23]), and parametric instability [24]. For a *flexible* guideway that permits vehicle-guideway interaction, additional sources of dynamic instability include: moving-object instability at super-critical velocities, referred to as wave-induced instability [2,25–32], parametric instability in periodically supported infinite guideways [11–13], parametric instability in finite structures periodically traversed by moving objects [33–35], and combination instability [33].

It becomes clear that when combining a highly flexible guideway with an advanced vehicle control system, it is essential to identify and study the relevant instability mechanisms. In particular, understanding the parameter combinations and velocity ranges that may lead to instability in Maglev and Hyperloop systems (i.e., determining critical velocities [2,25,28,30–32,36–38]) is crucial for their design and practical implementation. This study aims to determine the said unstable velocity regimes, and, more specifically, is concerned with the interaction of two instability sources, namely (i) the improperly controlled electromagnetic suspension, and (ii) the wave-induced instability. To achieve this, the Maglev/Hyperloop system is modeled as an infinite beam supported by a visco-elastic foundation subjected to a moving mass (see Fig. 1). The vehicle-guideway interaction is mediated by a nonlinear electromagnetic force governed by the suspension system. The electromagnetic suspension inherently destabilizes the system, necessitating a control strategy to ensure stability even at quasi-static velocities. In this work, a basic proportional and derivative (PD) control strategy with constant gains is employed.

The novelty of this work lies in bridging the structural-dynamics and control-dynamics aspects of the problem. From a *structural-dynamics* perspective, the influence of the electromagnetic suspension on the stability of an object moving on an infinite guideway has not been previously explored. From a *control-dynamics* perspective, the guideway is often simplified to either a rigid base [23,39] or a single-degree-of-freedom (SDOF) system [17,40], thereby neglecting the vehicle-velocity dependent nature of the guideway reaction force. The few studies that include a flexible guideway consider it as a finite bridge-like structure (e.g., [33–35,41–45]), and are, thus, unable to capture the wave-induced instability mechanism. This study makes the first attempt to combine these two aspects and investigate the interaction between two fundamentally different sources of instability. Additionally, this study introduces a methodology to distinguish the contributions of each instability mechanism to the overall system stability. More specifically, the energy variation of the vehicle is divided in two components corresponding to (i) energy input by the electro-magnetic suspension and (ii) energy input by the guideway. While identifying unstable velocity regimes is practical for Hyperloop design, the ability to discern which mechanism causes system instability for a certain parameter combination is valuable can be crucial for efficient mitigation.

This study begins by presenting the nonlinear model representative of Maglev/Hyperloop systems in Section 2, followed by the numerical solution method used to analyze this model in Section 3. Section 4 introduces the two system equilibria, the linearized model, and the derivation of its eigenvalues. These eigenvalues are used to predict stability boundaries, while the numerical solution of the nonlinear system explores the presence of limit-cycle oscillations. Section 5 investigates the stability of both equilibria at quasi-static vehicle velocities, examining stability boundaries, limit cycles, and basins of attraction. Section 6 focuses on how vehicle velocity affects the stability of the relevant equilibrium, particularly the interaction between electromagnetic and wave-induced instability (the latter occurring only at super-critical velocities). To differentiate the contribution of each instability mechanism, Section 7 introduces an energy analysis method. These last two sections represent the primary novel contributions of this work.

2. Model formulation

The system consists of an infinite Euler–Bernoulli beam with mass per unit length ρ and bending stiffness EI. The beam is continuously supported by distributed springs (k_d) and dashpots (c_d). The guideway is acted upon by a vehicle of mass M moving with velocity v. The vehicle and the guideway are connected through a nonlinear electromagnetic force F that, similarly to the

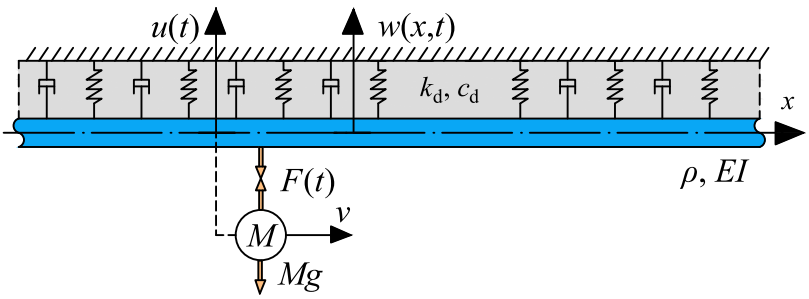

Fig. 1. System schematics: an infinite Euler–Bernoulli beam continuously supported by a visco-elastic foundation subject to a moving mass. The vehicle–structure interaction is governed by the nonlinear electromagnetic suspension.

electromagnetic suspension in Maglev trains, only works in attraction [23]. For the chosen solution method, it is convenient to write the governing equations in the reference frame moving with the vehicle, i.e., $\xi = x - vt$ and $\tau = t$, where (x,t) and (ξ,τ) are the spatial and temporal coordinates in the stationary and moving reference frames, respectively. Fig. 1 depicts the system, while its governing equations read [23]

$$EI\frac{\partial^4 w}{\partial \xi^4} + \rho\left(\frac{\partial^2 w}{\partial \tau^2} - 2v\frac{\partial^2 w}{\partial \xi \partial \tau} + v^2\frac{\partial^2 w}{\partial \xi^2}\right) + c_\mathrm{d}\left(\frac{\partial w}{\partial \tau} - v\frac{\partial w}{\partial \xi}\right) + k_\mathrm{d} w = -F(\tau)\delta(\xi), \tag{1}$$

$$M\frac{\mathrm{d}^2 u}{\mathrm{d}\tau^2} = F(\tau) - Mg, \tag{2}$$

$$F(\tau) = C\frac{I^2}{\left(w_0 - u\right)^2}, \tag{3}$$

$$\frac{\mathrm{d}I}{\mathrm{d}\tau} = \frac{w_0 - u}{2C}\left[U(\tau) - IR + 2C\frac{I}{\left(w_0 - u\right)^2}\left(\frac{\mathrm{d}w_0}{\mathrm{d}\tau} - \frac{\mathrm{d}u}{\mathrm{d}\tau}\right)\right], \tag{4}$$

$$U(\tau) = K_\mathrm{p}\left(w_0 - u - \Delta_\mathrm{targ}\right) + K_\mathrm{d}\left(\frac{\mathrm{d}w_0}{\mathrm{d}\tau} - \frac{\mathrm{d}u}{\mathrm{d}\tau}\right) + U_\mathrm{targ}, \tag{5}$$

where g is the gravitational acceleration, δ represents the Dirac delta function, u is the mass displacement (measured from the undeformed beam position), and $w_0(\tau) = w(\xi = 0, \tau)$ is the beam displacement under the moving mass. The electromagnetic force F depends on the current intensity I and on the air-gap $\Delta = w_0 - u$, while C is a constant that depends on the electro-magnet properties [23]. Eq. (4) is a nonlinear differential equation governing the current intensity where U is the voltage and R is the circuit resistance. Note that F represents just the lift component of the electromagnetic force while the drag component is neglected. Also, the velocity dependency of the lift component [39] is neglected and could be investigated in future studies.

Without a control strategy, the formulated system is inherently unstable, even when the vehicle is not moving. Consequently, a control strategy on voltage U is imposed (Eq. (5)). A standard proportional and derivative control strategy is used, where K_p and K_d are the position and velocity feedback gains, respectively. The error is defined as the deviation from the target air-gap Δ_targ (subscript targ stands for target); U_targ represents the voltage that leads to the target air-gap at equilibrium. More complex control strategies can be implemented, but for this investigation, the simple control strategy suffices.

We consider a typical Hyperloop design that was previously described in [46]. Since the current model neglects the discrete nature of the supports, the relevant parameters from [46] are divided by the support spacing to obtain an equivalent distributed foundation. The vehicle is suspended from above and the displacement w is at the rail level (located at the top of the tube). Consequently, the spring stiffness in our phenomenological model accounts not only for the support stiffness, but also for the flexibility of the tube–rail connection and, most importantly, for the flexibility introduced by the ovalization of the tube. The parameter values are $EI = 25{\times}10^6$ kNm^2, $\rho = 1400$ kg/m, $k_\mathrm{d} = 28 \times 10^3$ kN/m^2, $c_\mathrm{d} = 20$ kNs/m^2, $M = 7650$ kg, $C = 0.05$ Nm^2/A^2, and $\Delta_\mathrm{targ} = 15$ mm. The foundation damping c_d is chosen such that the damping ratio (defined as in Ref. [47]) is 5%.

3. Numerical solution of the nonlinear system

Since the system stability is dictated by the vehicle-guideway interaction, it suffices to investigate the response under the moving vehicle (i.e., $\xi = 0$). To this end, the guideway response w_0 under the moving vehicle is written as follows [48,49]:

$$w_0(\tau) = -\int_0^\tau G_0(\tau - \theta)F(\theta)\mathrm{d}\theta + w_0^{\mathrm{ic}}(\tau), \qquad \tau \geq 0, \tag{6}$$

where θ is the running time variable, G_0 represents the guideway response (or Green's function) evaluated at $\xi = 0$ to a moving impulse load (i.e., $\delta(\tau)\delta(\xi)$) while $w_0^{\mathrm{ic}}(\tau)$ represents the free-vibration response of the guideway at $\xi = 0$ due to the imposed initial conditions. The latter term is necessary because the convolution integral captures just the response of the system with trivial initial

conditions. Note that obtaining Eq. (6) from Eq. (1) required no assumptions or approximations, with the only restriction that Eq. (6) limits the observation to the position of the vehicle. Also, the partial-differential equation of the beam is not explicit in Eq. (6), but is accounted for through the non-local (in time) nature of the Green's function G_0.

The Green's function G_0 can be obtained from Eq. (1) by replacing $-F(\tau)$ with $\delta(\tau)$. The ensuing equation can be solved by applying the Laplace transform over time and expressing the Laplace-domain solution as a superposition of wave modes [48]. The resulting analytical solution is evaluated at $\xi = 0$ to obtain $\hat{G}_0$ (the hat indicates that the quantity belongs to the Laplace domain). Its time-domain counterpart G_0 is obtained by evaluating the inverse Laplace transform numerically.

To solve the system of Eqs. (2)–(6), we first approximate the convolution integral by discretizing time and assuming a linear variation of the electromagnetic force inside one time step, obtaining the following expression [50]:

$$w_{0,n} = \sum_{\bar{n}=0}^{n-1}\left[F_{\bar{n}}\left(w_{0,\bar{n}}\right)\mathcal{L}_{n-\bar{n}-1} + F_{\bar{n}+1}\left(w_{0,\bar{n}+1}\right)\mathcal{R}_{n-\bar{n}-1}\right] + w_{0,n}^{\mathrm{ic}}, \qquad n \geq 1, \tag{7}$$

$$\mathcal{L}_{n-\bar{n}-1} = \int_{\tau_{\bar{n}}}^{\tau_{\bar{n}+1}} G_0(\tau_n - \theta)\left(1 - \frac{\theta - \tau_{\bar{n}}}{\Delta\tau}\right)\mathrm{d}\theta, \tag{8}$$

$$\mathcal{R}_{n-\bar{n}-1} = \int_{\tau_{\bar{n}}}^{\tau_{\bar{n}+1}} G_0(\tau_n - \theta)\frac{\theta - \tau_{\bar{n}}}{\Delta\tau}\mathrm{d}\theta, \tag{9}$$

where n is the observation time index while $\bar{n}$ is the running (integration) time index. Eq. (7) is valid only for $n \geq 1$ because the response is described by the initial conditions (incorporated in $w_{0,n}^{\mathrm{ic}}$) at $\tau_0 = 0$. $\mathcal{L}$ and $\mathcal{R}$ represent the responses observed at τ_n due to triangular pulses lasting between $\tau_{\bar{n}}$ and $\tau_{\bar{n}+1}$.

Eq. (7) is implicit for $\bar{n} = n - 1$ because the contact force F_n depends on the response $w_{0,n}$. Therefore, the equation is divided in a yet unknown *instantaneous* contribution and an already known *history* term, leading to

$$w_{0,n} = w_{0,n}^{\mathrm{ic}} + w_{0,n}^{\mathrm{hist}} + F_n\left(w_{0,n}\right)\mathcal{R}_0, \tag{10}$$

$$w_{0,n}^{\mathrm{hist}} = \sum_{\bar{n}=0}^{n-2}\left[F_{\bar{n}}\left(w_{0,\bar{n}}\right)\mathcal{L}_{n-\bar{n}-1} + F_{\bar{n}+1}\left(w_{0,\bar{n}+1}\right)\mathcal{R}_{n-\bar{n}-1}\right] + F_{n-1}\left(w_{0,n-1}\right)\mathcal{L}_0.$$

Next, F_n (discretized Eq. (3)) is substituted in Eq. (10), resulting in the third-order polynomial

$$w_{0,n}^3 + a_{2,n}w_{0,n}^2 + a_{1,n}w_{0,n} + a_{0,n} = 0, \tag{11}$$

$$a_{2,n} = -w_{0,n}^{\mathrm{ic}} - w_{0,n}^{\mathrm{hist}}, \quad a_{1,n} = -u_n^2, \quad a_{0,n} = \left(w_{0,n}^{\mathrm{ic}} - w_{0,n}^{\mathrm{hist}}\right)u_n^2 + CI_n^2\mathcal{R}_0.$$

The roots of this polynomial can be computed using a symbolic mathematical software (e.g., Maple) and are not given here for brevity. From the three existing roots, only one is physically admissible (i.e., real-valued and corresponding to the vehicle below the guideway). The discretized system of equations now reads

$$w_{0,n} = f(w_{0,n}^{\mathrm{ic}}, w_{0,n}^{\mathrm{hist}}, u_n, I_n), \tag{12}$$

$$M\ddot{u}_n = C\frac{I_n^2}{\left(w_{0,n} - u_n\right)^2} - Mg, \tag{13}$$

$$\dot{I}_n = \frac{w_{0,n} - u_n}{2C}\left[U_n - I_nR + 2C\frac{I_n}{\left(w_{0,n} - u_n\right)^2}\left(\dot{w}_{0,n} - \dot{u}_n\right)\right], \tag{14}$$

$$U_n = K_{\mathrm{p}}\left(w_{0,n} - u_n - \Delta_{\mathrm{targ}}\right) + K_{\mathrm{d}}\left(\dot{w}_{0,n} - \dot{u}_n\right) + U_{\mathrm{targ}}, \tag{15}$$

where f represents the expression of the real-valued root of Eq. (11), and the overdots represent time derivatives of the time-discretized variables. The resulting system of ordinary differential equations is solved through a time-stepping scheme (i.e., Runge–Kutta solver implemented in Matlab).

4. Linearization of the nonlinear system and eigenvalue analysis

To assess system stability, in addition to the numerical solution, it is helpful to examine the linearized system around the equilibrium state(s). Since the guideway (Eq. (1)) is homogeneous and the only external force, the vehicle's dead weight, remains constant over time, the electromagnetic force at equilibrium is $F_{\mathrm{ss}} = Mg$. This allows us to determine the equilibrium state(s) by analyzing the guideway and vehicle separately.

The guideway under the action of a moving constant electromagnetic force F_{ss} has a single equilibrium state, the so-called eigenfield (see Ref. [51]). The guideway equilibrium evaluated under the moving constant force is denoted by $w_{0,\mathrm{ss}}$. The vehicle, however, has two equilibria for the same constant electromagnetic force F_{ss}. The two equilibria are obtained by solving the following nonlinear algebraic system of equations

$$\frac{I^2}{\left(w_{0,\mathrm{ss}} - u\right)^2} = \frac{Mg}{C}, \tag{16}$$

$$K_{\mathrm{p}}(w_{0,\mathrm{ss}} - u - \Delta_{\mathrm{targ}}) + U_{\mathrm{targ}} - IR = 0. \tag{17}$$

Solving the above set of equations for u and I ($w_{0,\mathrm{ss}}$ is known) leads to two equilibrium states: $[w_{0,\mathrm{ss}}, 0, u_{\mathrm{ss},1}, 0, I_{\mathrm{ss},1}]$ and $[w_{0,\mathrm{ss}}, 0, u_{\mathrm{ss},2}, 0, I_{\mathrm{ss},2}]$, where the second and fourth entries correspond to the beam and mass velocities which are zero at equilibrium. The explicit expressions are omitted for brevity, but they can be obtained straightforwardly by solving the above system of equations using a symbolic solver (e.g., Maple or Mathematica).

The yet unknown target voltage U_{targ} can be now determined by equating either of the two steady-state air-gaps to the target air-gap: $\Delta_{\mathrm{ss},1/2} = w_{0,\mathrm{ss}} - u_{\mathrm{ss},1/2} = \Delta_{\mathrm{targ}}$. This condition results in the following solutions (irrespective if one uses the first or second equilibrium for u and I):

$$U_{\mathrm{targ}} = \pm\sqrt{\frac{Mg}{C}}R\Delta_{\mathrm{targ}}. \tag{18}$$

From practical considerations, the positive-definite U_{targ} is chosen. This choice leads to the first equilibrium air-gap matching the target value, i.e., $\Delta_{\mathrm{ss},1} = \Delta_{\mathrm{targ}}$, while the second equilibrium air-gap does not, i.e., $\Delta_{\mathrm{ss},2} \neq \Delta_{\mathrm{targ}}$.

With the equilibrium states determined, the nonlinear system is linearized around each one separately to assess their stability. To this end, a perturbation around each steady state is introduced by substituting $w_0(\tau) = w_{0,\mathrm{ss}} + w_{0,\mathrm{tr}}(\tau)$, $w_0^{\mathrm{ic}}(\tau) = w_{0,\mathrm{ss}}^{\mathrm{ic}} + w_{0,\mathrm{tr}}^{\mathrm{ic}}(\tau)$, $u(\tau) = u_{\mathrm{ss}} + u_{\mathrm{tr}}(\tau)$, $F(\tau) = F_{\mathrm{ss}} + F_{\mathrm{tr}}(\tau)$, $I(\tau) = I_{\mathrm{ss}} + I_{\mathrm{tr}}(\tau)$, where subscript tr stands for transient. Note that $w_0^{\mathrm{ic}}(\tau)$ is the free-vibration response of the guideway to initial conditions corresponding to $w_{0,\mathrm{ss}}^{\mathrm{ic}} + w_{0,\mathrm{tr}}^{\mathrm{ic}}(\tau)$; this quantity is not an unknown variable and is determined a-priori. After mathematical manipulations, we apply the Taylor expansion to the governing equations corresponding to Eqs. (3) and (4). Thus, the linearized system is obtained and reads

$$w_{0,\mathrm{tr}}(\tau) = -\int_0^{\tau} G_0(\tau-\theta)F_{\mathrm{tr}}(\theta)\mathrm{d}\theta + w_{0,\mathrm{tr}}^{\mathrm{ic}}(\tau), \qquad \tau \geq 0, \tag{19}$$

$$M\frac{\mathrm{d}^2 u_{\mathrm{tr}}}{\mathrm{d}\tau^2} = F_{\mathrm{tr}}(\tau), \tag{20}$$

$$F_{\mathrm{tr}}(\tau) = \frac{2CI_{\mathrm{ss}}^2}{\Delta_{\mathrm{ss}}^3}\left(\frac{\Delta_{\mathrm{ss}}}{I_{\mathrm{ss}}}I_{\mathrm{tr}} + u_{\mathrm{tr}} - w_{0,\mathrm{tr}}\right), \tag{21}$$

$$\frac{\mathrm{d}I_{\mathrm{tr}}}{\mathrm{d}\tau} = \frac{1}{2C}\left[-I_{\mathrm{tr}}R + \Big(K_{\mathrm{p}}(2\Delta_{\mathrm{ss}} - \Delta_{\mathrm{targ}}) - (I_{\mathrm{ss}}R - U_{\mathrm{targ}})\Big)\Big(w_{0,\mathrm{tr}} - u_{\mathrm{tr}}\Big) + \frac{K_{\mathrm{d}}\Delta_{\mathrm{ss}}^2 + 2CI_{\mathrm{ss}}}{\Delta_{\mathrm{ss}}}\left(\frac{\mathrm{d}w_{0,\mathrm{tr}}}{\mathrm{d}\tau} - \frac{\mathrm{d}u_{\mathrm{tr}}}{\mathrm{d}\tau}\right)\right]. \tag{22}$$

The equilibrium stability can be investigated through the eigenvalues of the linearized system. To obtain the characteristic equation, the Laplace transform is applied to Eqs. (19)–(22) with respect to time. The expression of the electromagnetic force is substituted in the Laplace-domain counterparts of Eqs. (19) and (20), and the resulting system of equations, in matrix form, reads

$$\begin{pmatrix} 1 - \hat{G}_0(s)\frac{2CI_{\mathrm{ss}}^2}{\Delta_{\mathrm{ss}}^3} & \hat{G}_0(s)\frac{2CI_{\mathrm{ss}}^2}{\Delta_{\mathrm{ss}}^3} & \hat{G}_0(s)\frac{2CI_{\mathrm{ss}}}{\Delta_{\mathrm{ss}}^2} \\ \frac{2CI_{\mathrm{ss}}^2}{\Delta_{\mathrm{ss}}^3} & Ms^2 - \frac{2CI_{\mathrm{ss}}^2}{\Delta_{\mathrm{ss}}^3} & -\frac{2CI_{\mathrm{ss}}}{\Delta_{\mathrm{ss}}^2} \\ \hat{f}(s) & -\hat{f}(s) & \frac{R\Delta_{\mathrm{ss}}}{2C} + s \end{pmatrix}\begin{pmatrix} \hat{w}_{0,\mathrm{tr}} \\ \hat{u}_{\mathrm{tr}} \\ \hat{I}_{\mathrm{tr}} \end{pmatrix} = \begin{pmatrix} \hat{w}_{0,\mathrm{tr}}^{\mathrm{ic}}(s) \\ M\left(su_{\mathrm{tr}}(\tau=0) + \frac{\mathrm{d}u_{\mathrm{tr}}}{\mathrm{d}\tau}\Big|_{\tau=0}\right) \\ \hat{q} \end{pmatrix}, \tag{23}$$

$$\hat{f}(s) = -\frac{K_{\mathrm{p}}(2\Delta_{\mathrm{ss}} - \Delta_{\mathrm{targ}}) - (I_{\mathrm{ss}}R - U_{\mathrm{targ}}) + \frac{(K_{\mathrm{d}}\Delta_{\mathrm{ss}}^2 + 2CI_{\mathrm{ss}})s}{\Delta_{\mathrm{ss}}}}{2C}, \tag{24}$$

$$\hat{q} = \frac{K_{\mathrm{d}}\Delta_{\mathrm{ss}}^2 + 2CI_{\mathrm{ss}}}{2C\Delta_{\mathrm{ss}}}\big(u_{\mathrm{tr}}(\tau=0) - w_{0,\mathrm{tr}}(\tau=0)\big) + I_{\mathrm{tr}}(\tau=0), \tag{25}$$

where $u_{\mathrm{tr}}(\tau=0)$, $\frac{\mathrm{d}u_{\mathrm{tr}}}{\mathrm{d}\tau}\Big|_{\tau=0}$, and $I_{\mathrm{tr}}(\tau=0)$ are the initial conditions of the perturbation for the mass and current while the beam perturbation is accounted for in $\hat{w}_{0,\mathrm{tr}}^{\mathrm{ic}}(s)$ and $w_{0,\mathrm{tr}}(\tau=0)$. For the stability analysis, the characteristic matrix given in Eq. (23) needs to be evaluated at the corresponding equilibrium state that is being investigated (i.e., ss,1 and ss,2).

The characteristic equation, which is not presented here for brevity, is obtained by equating the determinant of the characteristic matrix to zero. It must be emphasized that the characteristic equation is neither a polynomial (since s appears also in $\hat{G}_0$ under square roots) nor a transcendental equation, meaning that it has a finite amount of roots. The eigenvalues are determined numerically by using a root finding routine (i.e., *fsolve* in Matlab) with a multitude of initial guesses for s to cover the part of the complex plane relevant for this problem.

5. Stability investigation for quasi-static vehicle velocity

We begin by analyzing the stability of both equilibrium states in the quasi-static vehicle velocity regime (i.e., $v = 0.1c_{\mathrm{cr}}$), establishing a foundation for examining the effect of vehicle velocity on stability, which is addressed in the following section. In this paper, the critical velocity $c_{\mathrm{cr}} = \sqrt[4]{4k_{\mathrm{d}}EI/\rho^2}$ (this expression is only valid in the absence of damping; see Ref. [52] for a detailed derivation) refers to the minimum phase velocity of the guideway, at which the system experiences resonance, and not to the velocity at which stability is lost; in a non-dispersive medium such as air, c_{cr} corresponds to the speed of sound. It is important to highlight that the instability observed in all cases discussed in this section is solely due to inadequate control of the electromagnetic levitation system, as wave-induced instability cannot occur at sub-critical velocities in this system.

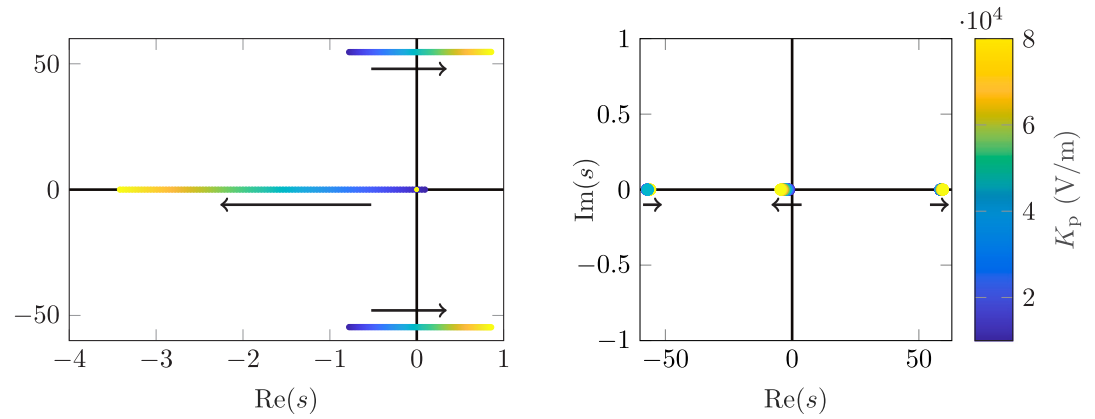

Fig. 2. Argand diagram of the eigenvalues for the linearized system around the first (ss,1; left panel) and second (ss,2; right panel) equilibrium as a function of K_p at quasi-static vehicle velocity ($v = 0.1c_{cr}$) with $K_d = 20$ (kVs/m). The arrows direction indicates increasing K_p value. (For interpretation of the colors in this figure, the reader is referred to the online version of this article.).

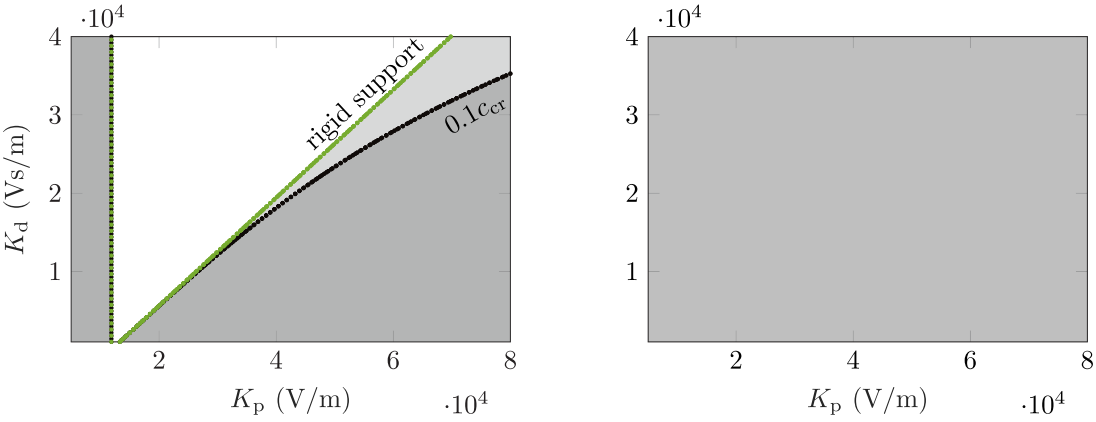

Fig. 3. Stability boundaries (black lines) vs control gains for the first (ss,1; left panel) and second (ss,2; right panel) equilibria for quasi-static vehicle velocity (i.e., $v = 0.1c_{cr}$), and the stability boundaries (green lines) vs control gains for the system with rigid support (i.e., rigid guideway). The white/gray background indicates stability/instability. (For interpretation of the colors in this figure, the reader is referred to the online version of this article.).

Fig. 2 shows the eigenvalues of the linearized system around each equilibrium as a function of K_p. For each equilibrium, three eigenvalues are identified, in contrast to studies that approximate the guideway as a single-degree-of-freedom system, which yield five eigenvalues [17,40]. For the first equilibrium (with $\Delta_{ss,1} = \Delta_{targ}$), the system exhibits a real-valued and two complex-conjugate eigenvalues. At low K_p, the real-valued eigenvalue is positive, indicating an unstable equilibrium (i.e., divergent instability). As K_p increases, the real-valued eigenvalue becomes negative, stabilizing the system. However, at sufficiently large K_p, the system undergoes a supercritical Hopf-like bifurcation, where the real part of the complex-conjugate eigenvalues becomes positive.

For the second equilibrium (with $\Delta_{ss,2} \neq \Delta_{targ}$), three real-valued eigenvalues are observed among which at least one is positive, indicating a saddle–node equilibrium. It is worth noting that for very small K_d and large K_p, two of the real-valued eigenvalues convert into a complex-conjugate pair, although this occurs at unrealistic values of K_p and is not shown here.

Fig. 3 shows the stability boundaries and regions for both equilibria in the control gain parameter space. For the first equilibrium, the position is unstable for all values of K_d when $K_p < K_{p,min} = R\sqrt{Mg/C}$, indicated by the left vertical line. For a detailed derivation of $K_{p,min}$ see Ref. [18] (Eq. (9) with the aero-elastic coefficient $\mu = 0$). When $K_p > K_{p,min}$, the equilibrium position becomes conditionally stable, depending on the combination of K_p and K_d. The right stability curve corresponds to the Hopf-like bifurcation, where the real part of the complex-conjugate eigenvalues becomes positive. For the second equilibrium, at least one positive real-valued eigenvalue is present for all values of K_p and K_d, making the equilibrium unconditionally unstable.

Fig. 3 also compares the stability boundaries of the current system (flexible guideway and quasi-static vehicle velocity) to those obtained for a rigid guideway. While the two boundaries exhibit minor quantitative differences at large values of K_p and K_d, overall they show qualitatively similar behavior. Therefore, assuming a rigid guideway yields reasonable results at quasi-static vehicle velocity, at least concerning the dynamic stability.

Fig. 4 investigates the nonlinear system response (obtained by solving Eqs. (12)–(15)) for control-gain combinations representative of the system dynamic stability. Four representative regions are considered: left unstable regime (top row), stable regime

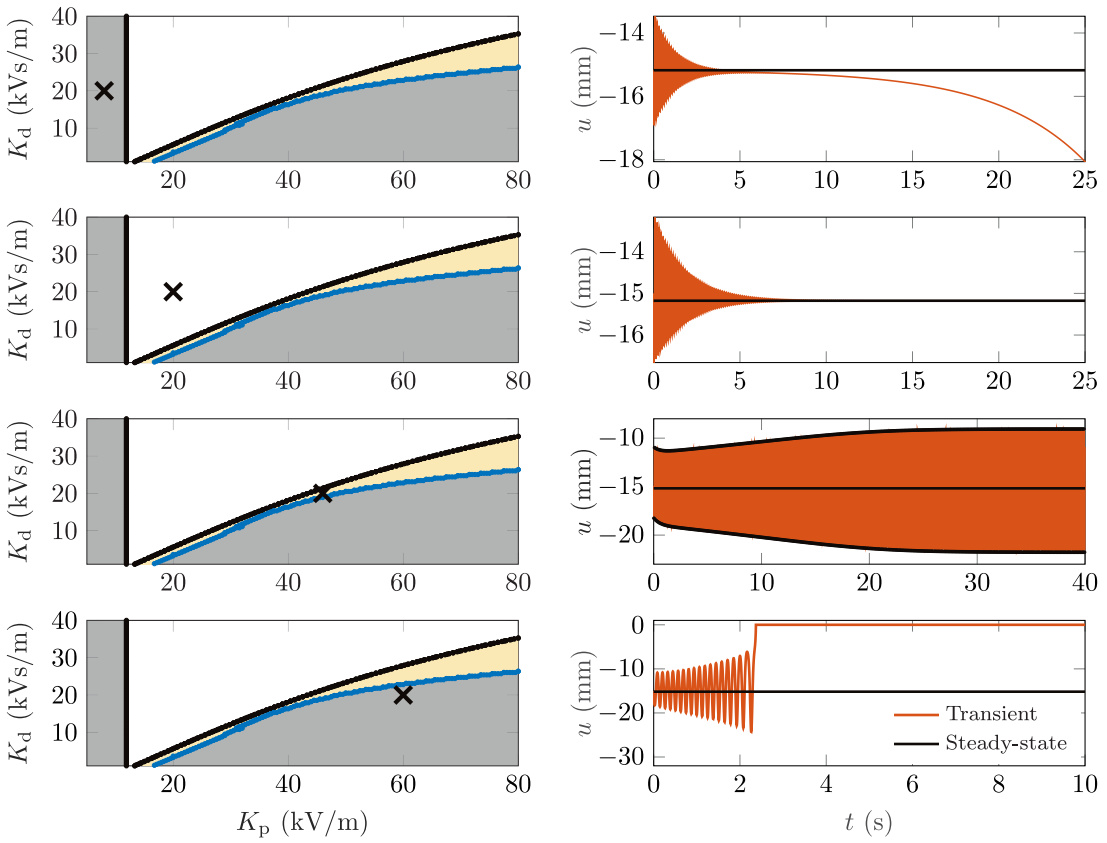

Fig. 4. Stability boundaries (black lines) versus control gains for the first equilibrium (ss,1; left panels) and the nonlinear time-history response of the mass (right panels) are presented for four representative control-gain combinations, indicated by the black cross. The region in which stable limit cycles are encountered is highlighted through the yellow background. The top row depicts the response in the left unstable regime, the second row shows the response in the stable regime, the third row illustrates the limit-cycle behavior just beyond the right stability boundary, and the bottom row displays the response in the right unstable regime. (For interpretation of the colors in this figure, the reader is referred to the online version of this article.).

(second row), stable limit-cycle regime (third row), and the right unstable regime (bottom row). The observations are summarized in the following:

- In the left unstable regime, the initial response exhibits a rapidly decaying oscillation due to the influence of the complex-conjugate eigenvalues with a negative real part. However, over time, the divergent nature of the equilibrium becomes dominant, resulting in an exponentially increasing response. In this scenario, the control system is too slow to prevent the vehicle from falling under the gravitational force.
- In the stable regime, the response oscillates around the equilibrium point with rapidly decreasing amplitude.
- Stable limit cycles are observed near the right stability boundary, as highlighted by the yellow background in Fig. 4. This region is relatively narrow and located close to the right stability boundary. During the limit-cycle oscillations, the electromagnetic force (not shown here for brevity) fluctuates between zero and a large value. This suggests that the oscillations are caused by an excessively aggressive control response, alternating between letting the vehicle free-fall and applying strong corrective forces.
- Well beyond the right stability boundary, limit cycles no longer exist. The control becomes excessively aggressive, causing it to overshoot, resulting in the vehicle colliding with the guideway, at which point the electromagnetic force becomes infinite.

While the control can stabilize the first equilibrium with the appropriate choice of gains, stability is only guaranteed for small perturbations. In practice, it is crucial to understand the allowable perturbations (e.g., guideway imperfections) that the design can safely accommodate. For sufficiently large perturbations, even if the first equilibrium is stable, the response could be pushed toward the unstable saddle–node equilibrium. Fig. 5 illustrates the separatrix between the two basins of attraction corresponding to the two equilibria, with one set of control gains within the stable regime (left panel) and another in the stable limit-cycle regime (right panel). These results are computed using the nonlinear model (see Section 3); each point in Fig. 5 represents a set of initial conditions, the green boundary separates the regions where trajectories lead to a stable equilibrium from those that result in instability.

Fig. 5 shows that the closer the vehicle is to the beam (i.e., smaller magnitude of u), the smaller the stable basin of attraction becomes. Conversely, as the vehicle moves further from the beam, the stable basin of attraction grows. Although the figure stops at

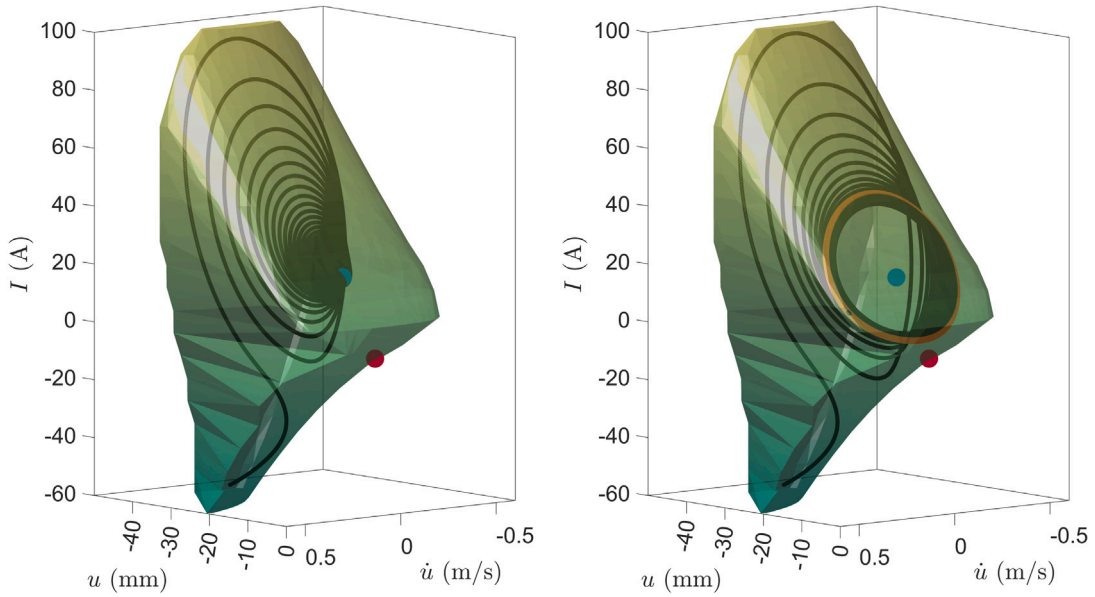

Fig. 5. Separatrix (green transparent boundary) between the two basins of attraction corresponding to the two equilibria (the first equilibrium is represented by the blue dot and the second by the red dot) for quasi-static vehicle velocity ($v = 0.1c_{cr}$). The left panel shows the case with $K_p = 30$ (kV/m) and $K_d = 20$ (kVs/m), corresponding to a stable spiral for the first equilibrium and a saddle node for the second. The right panel illustrates the case with $K_p = 46$ (kV/m) and $K_d = 20$ (kVs/m), where the first equilibrium is an unstable spiral but has a stable limit cycle (orange line) nearby, while the second equilibrium remains a saddle node. For clarity, one trajectory is included in each panel. (For interpretation of the colors in this figure, the reader is referred to the online version of this article.).

$u = -42$ mm, the basin extends beyond this point. Interestingly, the largest stable basin in the u–$\dot{u}$ space occurs for $I(t = 0) = 0$, not for $I(t = 0) = I_{ss,1}$. Notably, the stable basin of attraction is very similar in both scenarios (i.e., stable regime and stable limit-cycle regime), with only minor quantitative differences. This implies that most perturbations leading to equilibrium in the stable regime also result in limit cycles in the limit-cycle regime.

6. The influence of the vehicle velocity on the system stability

Although qualitatively similar results to those presented for quasi-static vehicle velocity (see previous section) could have been achieved using a rigid support model (e.g., [23,39]) or by approximating the guideway as a single-degree-of-freedom system (e.g., [17,40]), such models do not allow for investigating the influence of vehicle velocity on system stability. Properly accounting for the guideway makes this investigation possible, which is the focus of this section.

Fig. 6 presents the eigenvalues of the system linearized around the first equilibrium for fixed control gains K_p and K_d while varying the vehicle velocity. The results for the second equilibrium remain qualitatively similar to those for quasi-static velocity (see Section 5) and are thus omitted here.

The chosen control gains ensure system stability at quasi-static vehicle velocity. For part of the velocity range, three eigenvalues are observed, similar to the quasi-static case. However, in the velocity range of $v \approx 0.7$–$1.3c_{cr}$, an additional pair of complex-valued roots appears (not shown in Fig. 6), corresponding to branch points of the wavenumbers introduced by the dynamic stiffness of the infinite guideway. These are not eigenvalues of the system; the dynamics of infinite systems (guideway) coupled with finite/discrete ones (vehicle) cannot be fully captured by eigenvalues alone, as integrals along branch cuts also influence behavior. Nevertheless, neither the branch points nor the branch cut integrals affect system stability and are therefore excluded from this analysis. The observed jump in the location of the complex-valued eigenvalues around $v \approx 0.7c_{cr}$ is due to these eigenvalues crossing a branch cut.

Focusing on the three eigenvalues shown in Fig. 6, the real-valued eigenvalue remains nearly constant with varying velocity (as seen most clearly in the bottom left and right panels), while the complex-valued eigenvalues undergo significant changes. As velocity approaches c_{cr}, the negative real part of the complex-conjugate pair increases in magnitude, meaning that perturbation-induced vibrations decay more quickly as the vehicle velocity nears the critical value. This suggests that increasing velocity (within sub-critical limits) helps suppress perturbations. At approximately $1.3c_{cr}$, the real part of the complex-valued eigenvalues becomes positive, indicating that the equilibrium loses stability via a supercritical Hopf-type bifurcation. Interestingly, further increasing the velocity causes the equilibrium to regain stability. This behavior is not unique to controlled electromagnetic suspension systems, as it also occurs in analogous mechanical systems with compliant vehicle-guideway contact relations [37].

Regarding the stability boundaries, Fig. 7 illustrates the effect of vehicle velocity on these boundaries in the control gain parameter space. The unstable region where $K_p < K_{p,min}$ remains unaffected by changes in vehicle velocity. This is expected, as

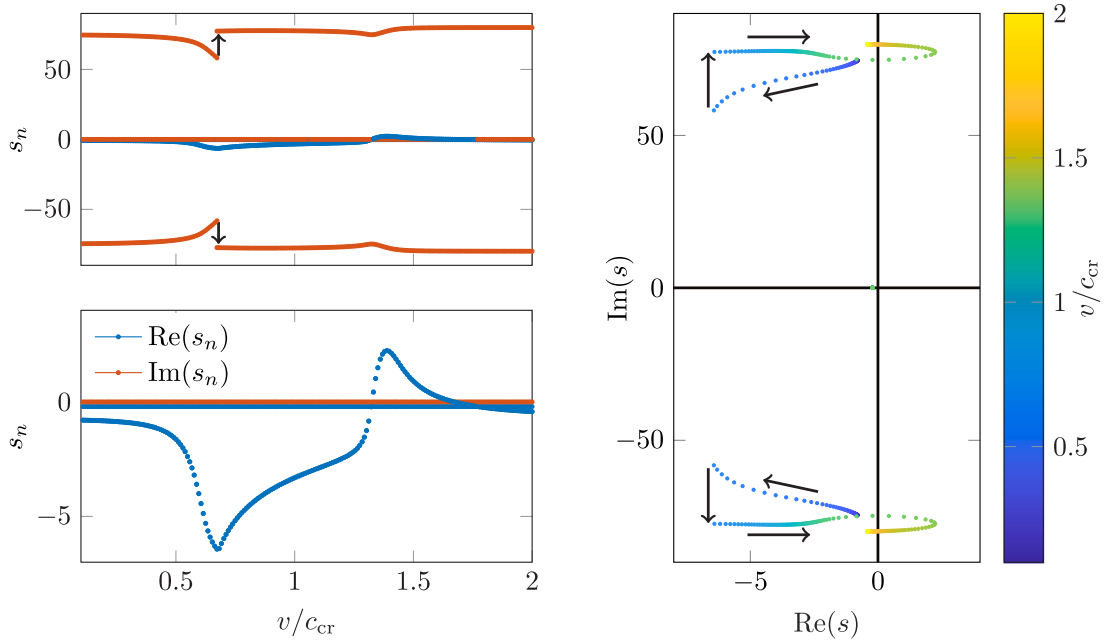

Fig. 6. The eigenvalues linearized around the relevant equilibrium (ss,1) versus vehicle relative velocity (left panels) and their Argand diagram (right panel). The bottom left panel is a zoom in of the top left panel. $K_p = 20$ (kV/m), $K_d = 40$ (kVs/m). The arrows direction indicates increasing velocity. (For interpretation of the colors in this figure, the reader is referred to the online version of this article.).

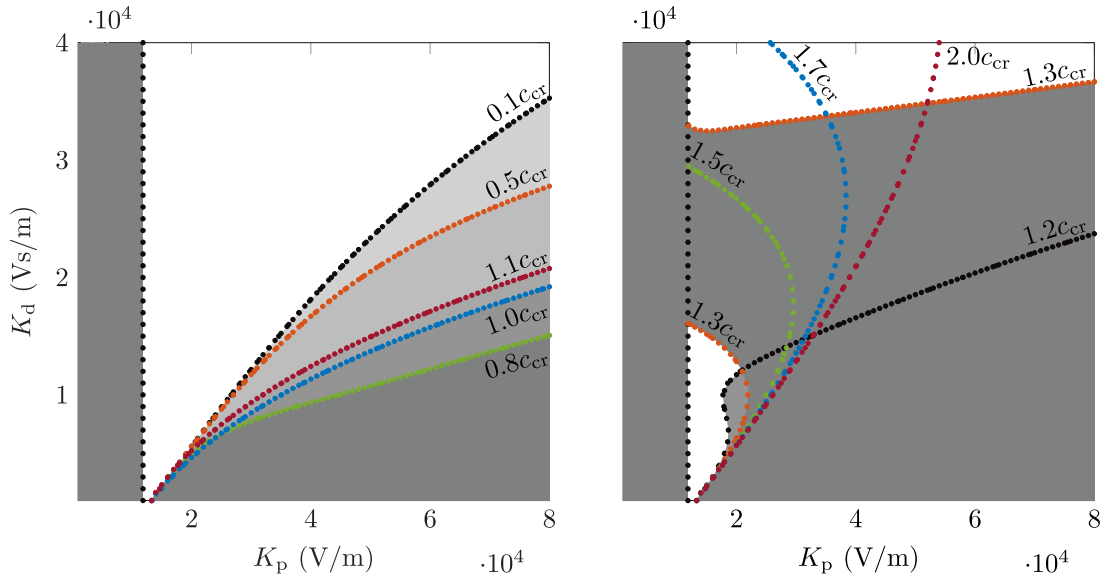

Fig. 7. Stability vs control gains for different vehicle velocities, namely $v = 0.1$–$1.1c_{cr}$ (left panel) and $v = 1.2$–$2c_{cr}$ (right panel); white/gray background indicates stability/instability. Note that for $v = 1.5$–$2c_{cr}$, the instability region is outside the closed ovals and does not have a gray background to avoid cluttering the figure. (For interpretation of the colors in this figure, the reader is referred to the online version of this article.).

this instability is entirely driven by the electromagnetic suspension, as shown by the expression for $K_{p,min} = R\sqrt{Mg/C}$, which depends solely on the electromagnetic properties and the vehicle's dead weight.

For $K_p > K_{p,min}$, the equilibrium position can become stable. The size of the stable domain increases monotonically with rising velocity, reaching its maximum at approximately $v \approx 0.8c_{cr}$. Beyond this point, it slightly decreases until $v \approx 1.1c_{cr}$. The instability observed in these cases (left panel of Fig. 7) is entirely due to inadequate control of the electromagnetic suspension system.

The shape of the stable domain undergoes significant changes starting at approximately $v \approx 1.2c_{cr}$ (right panel of Fig. 7) and reaches its minimum size at $v \approx 1.3c_{cr}$. While at lower velocities the stability domains expand or contract slightly without qualitative

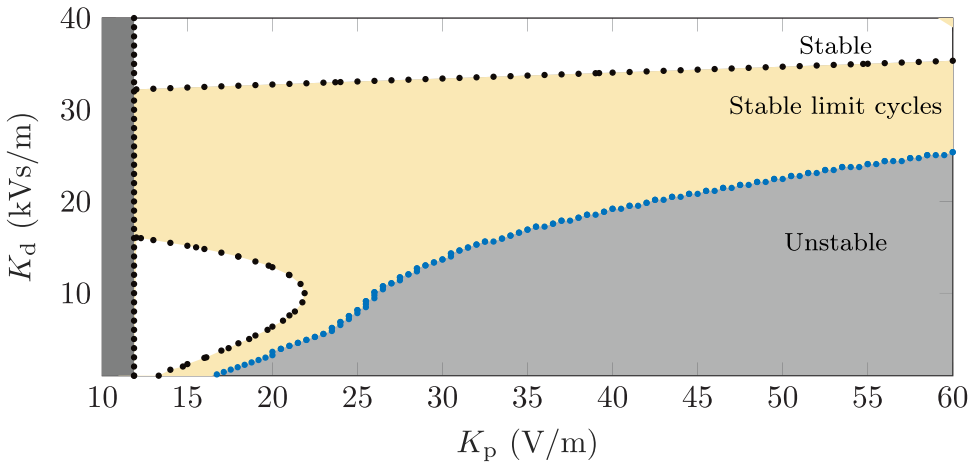

Fig. 8. Stability vs control gains for $v = 1.3c_{cr}$. White/gray background indicates stability/instability while the yellow background indicates the region in which stable limit cycles are encountered. (For interpretation of the colors in this figure, the reader is referred to the online version of this article.).

changes, at $v \approx 1.3c_{cr}$ and beyond, the stability domain transitions into a closed oval shape at higher velocities, with an additional stable region appearing above a certain K_d value (see the nearly horizontal line in the right panel). As the velocity increases further, the stable parameter space grows again through the expansion of the oval region. The shift in behavior between the left and right panels of Fig. 7 is not due to the control system, but rather the emergence of a second instability mechanism, the so-called wave-induced instability. Specifically, energy radiated by the vehicle into the guideway is fed back into the vehicle's vibration via anomalous Doppler waves [26].

It is important to note that, similar to its mechanical counterpart, this type of instability occurs only at super-critical velocities ($v > c_{cr}$). Additionally, this instability cannot be captured when the guideway is simplified to a single-degree-of-freedom system, as in previous studies on Maglev trains, and it can significantly reduce the stability parameter range.

Limit-cycle oscillations are encountered also in the velocity regime where wave-induced instability occurs. Fig. 8 highlights the region of stable limit cycles in the control gain parameter space for $v = 1.3c_{cr}$. Interestingly, while the stability boundary changed significantly above $v = 1.2c_{cr}$, the right boundary separating stable limit cycles and instability remains almost unchanged. This implies that the limit cycles are mostly governed by the electromagnetic control. It is worth mentioning that limit cycles are also observed in equivalent mechanical systems provided that either the contact force [2] or the guideway [53] has a nonlinear behavior. Nonetheless, limit cycles in mechanical systems are only observed at super-critical velocities because the radiated energy feedback is the sole instability mechanism, while the Hyperloop system exhibits limit cycles at any velocity (provided that K_p, K_d are chosen appropriately) due to the electromagnetic instability.

7. Energy analysis

The eigenvalue analysis presented in the previous section is straightforward and fully describes the system's stability, but it fails to differentiate between various instability sources. Consequently, discerning the primary contributing mechanism for effective mitigation remains impossible. To judge the contribution of different components to the stability of the system, we present hereafter an investigation based on the energy variation of the moving mass. It must be emphasized that the system linearized around the relevant (first) equilibrium is used for this investigation, as was used for the eigenvalue analysis. Also, the subscript tr is omitted in the following expressions for brevity.

7.1. Separating the two instability mechanisms

The variation of the moving mass energy E_M can be obtained by multiplying both sides of the equation of motion of the discrete mass (Eq. (20) without subscript tr) by its velocity $\frac{du}{d\tau}$. Re-writing the left-hand side as $M\frac{d^2u}{d\tau^2}\frac{du}{d\tau} = \frac{d}{d\tau}\frac{1}{2}M\left(\frac{du}{d\tau}\right)^2$, the following expression is obtained

$$\frac{d}{d\tau}E_M = F(\tau)\frac{du}{d\tau}, \qquad E_M = \frac{1}{2}M\left(\frac{du}{d\tau}\right)^2. \tag{26}$$

The guideway contribution to the vehicle energy variation is implicitly incorporated in $F(\tau)$. To express it explicitly, we add and subtract the term $F(\tau)\frac{dw_0}{d\tau}$ to the right-hand side of Eq. (26), thus obtaining

$$\frac{d}{d\tau}E_M = \underbrace{-F(\tau)\frac{d\Delta}{d\tau}}_{\text{Energy input } E_{em} \text{ by electromagnetic force}} + \underbrace{F(\tau)\frac{dw_0}{d\tau}}_{\text{Energy input } E_{gw} \text{ by the guideway}} \tag{27}$$

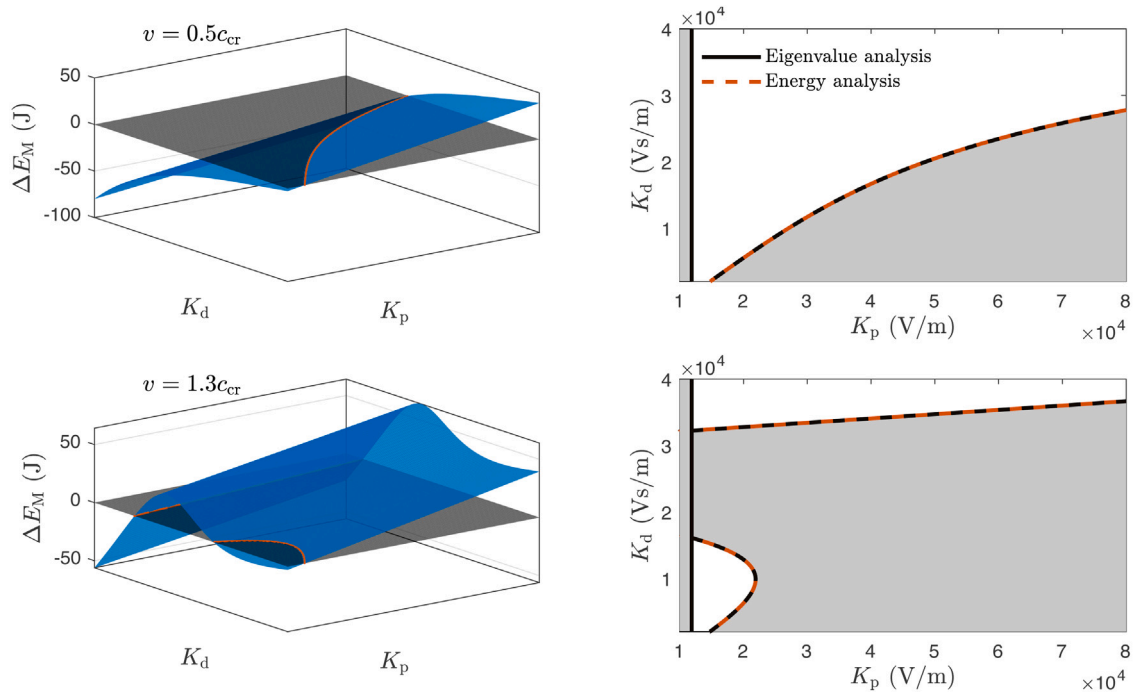

Fig. 9. ΔE_M (left panels) and $\Delta E_M = 0$ (right panels) in the K_p–K_d parameters space for two vehicle velocities: $v = 0.5c_{cr}$ (top panels) and $v = 1.3c_{cr}$ (bottom panels). The curves defined by $\mathrm{Re}(s_n) = 0$ from the eigenvalue analysis are superimposed in the right panels. In the right panels, the white/gray background indicates stability/instability. (For interpretation of the colors in this figure, the reader is referred to the online version of this article.).

Eq. (27) shows that there are two main contributions to the energy variation of the vehicle: (i) the energy input E_{em} by the electromagnetic force, and (ii) the energy input E_{gw} by the guideway. Positive input represents energy added to the mass vibration while negative input represents energy dissipation. Since both these contributors can cause instability, they can either dissipate or input energy into the vehicle vibration.

To identify the dominant instability mechanism using the linear system (Eqs. (19)–(22) linearized around ss,1), one approach is to analyze its response to a small perturbation and use it to calculate the terms in Eq. (27). However, to better illustrate the physical mechanism behind wave-induced instability (done in the next section), a different method is used. Instead of analyzing free vibration, we examine the steady-state response to an imposed harmonic motion of the moving mass, with the frequency Ω from the eigenvalue s determined in Sections 4–6. In other words, we examine the steady-state response to a harmonic excitation at the same frequency as the free-vibration response. The response to this system is derived in detail in Appendix A. Considering this system, the equilibrium state is unstable only if the energy variation averaged over one oscillation period is positive. The energy variation given in Eq. (27) averaged over one oscillation period reads

$$\Delta E_M = \overline{E}_{em} + \overline{E}_{gw}, \tag{28}$$

$$\Delta E_M = E_M(\tau + \Theta) - E_M(\tau), \qquad \overline{E}_{em} = -\frac{1}{\Theta}\int_0^{\Theta} F(\tau)\frac{\mathrm{d}\Delta}{\mathrm{d}\tau}\mathrm{d}\tau, \qquad \overline{E}_{gw} = \frac{1}{\Theta}\int_0^{\Theta} F(\tau)\frac{\mathrm{d}w_0}{\mathrm{d}\tau}\mathrm{d}\tau, \tag{29}$$

where the overbar indicates that the quantities have been averaged over one oscillation period $\Theta = \frac{2\pi}{\Omega}$.

A negative/positive ΔE_M indicates that the free-vibration response to a perturbation will decay/increase over time, which should align with the corresponding eigenvalue (from which the oscillation frequency Ω was used) having a negative/positive real part. A value of $\Delta E_M = 0$ marks the stability boundary. It may seem that the energy analysis does not provide additional insights into stability since it uses the eigenvalue analysis as input and only confirms the stability boundaries. However, the energy analysis also identifies which instability mechanism (i.e., which contributor from Eq. (27)) is dominant, allowing the instability to be attributed to one of the two mechanisms at play. Fig. 9 presents ΔE_M in the K_p–K_d parameter space for a sub-critical and a super-critical velocity. The resulting stability boundaries (i.e., curves defined by $\Delta E_M = 0$) match perfectly the ones obtained from the eigenvalues analysis (i.e., curves defined by $\mathrm{Re}(s_n) = 0$) when instability is caused by the complex-valued eigenvalue pair (i.e., stability is lost through a Hopf-type bifurcation). The left instability zone, caused by the real-valued eigenvalue being positive, is not captured by the energy analysis because this method assumes harmonic motion at the stability boundary, whereas the left boundary involves constant rigid-body motion, not harmonic oscillation. Nonetheless, the stability to the right of the left boundary is correctly predicted by the energy analysis, thus demonstrating that here the system stability is indeed governed by the energy variation expressed in Eq. (28).

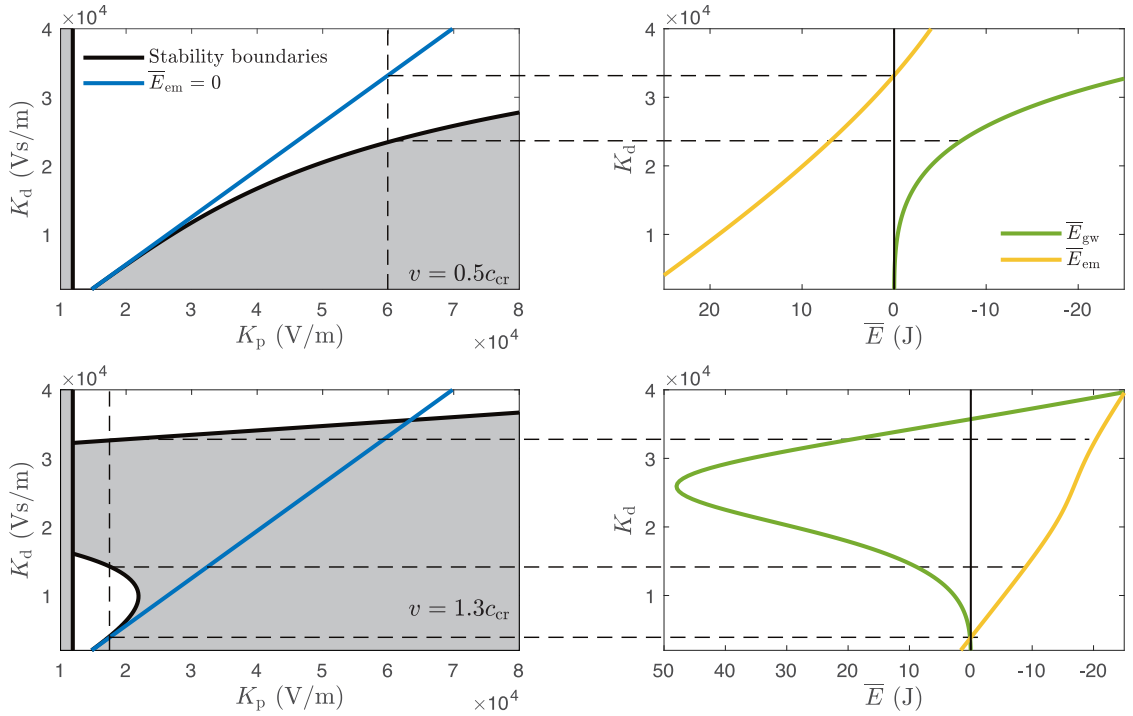

Fig. 10. Left panels: Stable/unstable domains in the K_p–K_d parameter space and the curve corresponding to no energy input by the electromagnetic force (i.e., $\overline{E}_{em} = 0$). Right panels: energy input by the electromagnetic force $\overline{E}_{em}$ and by the guideway $\overline{E}_{gw}$ vs K_d for one value of K_p indicated by the vertical dashed black line in the left panels. These results are presented for two vehicle velocities: $v = 0.5c_{cr}$ (top panels) and $v = 1.3c_{cr}$ (bottom panels). In the left panels, the white/gray background indicates stability/instability. (For interpretation of the colors in this figure, the reader is referred to the online version of this article.).

Furthermore, the domains where the eigenvalue analysis predicted instability (gray background) coincide with a positive ΔE_M, further validating the energy analysis.

Taking advantage of the energy analysis, Fig. 10 presents the separate contributions of the electromagnetic and wave-induced instability mechanisms. The contributions are presented along the K_d axis for one selected value of K_p (their 3-D representation in the K_p–K_d parameter space was considered unclear by the authors). To emphasize the influence of the guideway, the curve describing zero energy input by the electromagnetic force (i.e., $\overline{E}_{em} = 0$) is also presented; this curve represents the stability boundary for a rigid guideway [18,23,39].

On the one hand, the results for $v = 0.5c_{cr}$ demonstrate that the instability at sub-critical velocities is caused by the electromagnetic force having a positive energy input ($\overline{E}_{em} > 0$). The guideway, through its negative energy input (i.e., energy dissipation), proves to be a stabilizing mechanism and, consequently, enlarges the stability domain by bending downward the $\overline{E}_{em} = 0$ curve. On the other hand, the results for $v = 1.3c_{cr}$ show that, for a range of K_d, $\overline{E}_{gw}$ is positive and is the main cause of instability at super-critical velocities, while $\overline{E}_{em}$ is mainly negative, meaning the electromagnetic suspension is stabilizing. All in all, Fig. 10 demonstrates the competition and the complex interaction between the electromagnetic and wave-induced instability mechanisms, where each one can be a stabilizing or destabilizing mechanism depending on the vehicle velocity.

Finally, Fig. 11 illustrates the regions in the control-gain plane where each of the two instability mechanisms is either stabilizing or destabilizing for $v = 1.3c_{cr}$. It is evident that wave-induced instability is triggered across a significant portion of the control-gain plane (indicated by the orange and blue backgrounds), while the control strategy can counteract this effect only in limited areas (represented by the white regions in the left panel).

7.2. Anomalous Doppler waves

In the previous section, we distinguished between the two instability mechanisms: wave-induced instability (associated to the guideway contribution to the mass energy variation) and electromagnetic instability (associated to the electromagnetic force contribution to the mass energy variation). The question naturally arises as to how can the guideway (with positive viscous damping in the foundation) continuously provide energy to the vehicle in order to destabilize it. To demonstrate the physical mechanism of the wave-induced instability, the guideway contribution $\overline{E}_{gw}$ is divided into so-called normal and anomalous Doppler waves [26].

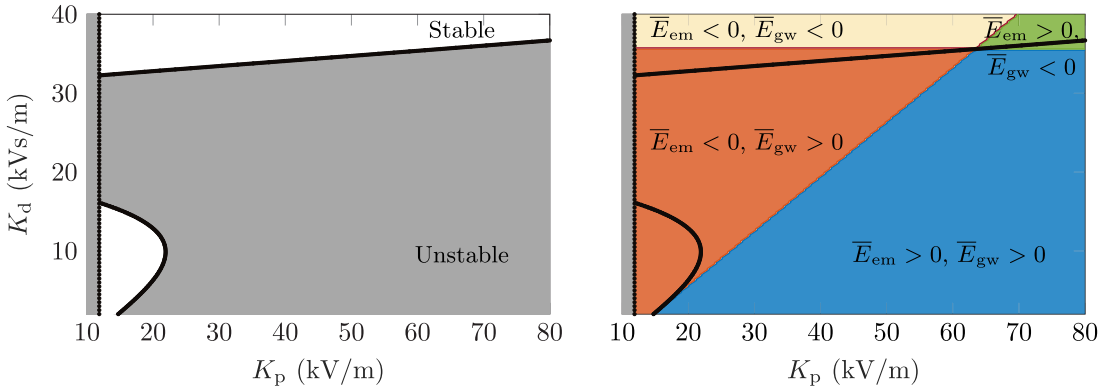

Fig. 11. Left panel: Stability vs control gains for $v = 1.3c_{cr}$; white/gray background indicates stability/instability. Right panel: the regions in the control-gain plane where (i) the electromagnetic suspension is destabilizing (i.e., $\overline{E}_{em} > 0, \overline{E}_{gw} < 0$; green background), (ii) the guideway is destabilizing (i.e., $\overline{E}_{em} < 0, \overline{E}_{gw} > 0$; orange background), (iii) both are destabilizing (i.e., $\overline{E}_{em} > 0, \overline{E}_{gw} > 0$; blue background), or (iv) none of them are destabilizing (i.e., $\overline{E}_{em} < 0, \overline{E}_{gw} < 0$; yellow background). (For interpretation of the colors in this figure, the reader is referred to the online version of this article.).

To facilitate this division, E_{gw} given by Eq. (27) needs to be expressed in terms of energy quantities radiated into the beam. To this end, E_{gw} is expressed based on its equation of motion as follows (Appendix B offers a detailed derivation):

$$E_{gw}(\tau) = F(\tau)\frac{dw_0}{d\tau} = \left(S_0^+ - vh_0^+\right) - \left(S_0^- - vh_0^-\right) + E_{F,h}(\tau), \tag{30}$$

where $S(\xi,\tau)$ and $h(\xi,\tau)$ represent wave energy flux and wave energy density, respectively, in the moving-reference frame (their expressions are given in Eqs. (B.13)–(B.14)), and $E_{F,h}(\tau)$ is the energy input by the horizontal force maintaining the constant vehicle velocity (for more details, see [51,54] and Appendix B). $S_0^+ = S(\xi = 0^+,\tau)$ and $h_0^+ = h(\xi = 0^+,\tau)$ represent the quantities evaluated just ahead of the moving mass, while $S_0^- = S(\xi = 0^-,\tau)$ and $h_0^- = h(\xi = 0^-,\tau)$ are the quantities evaluated just behind the moving mass.

The expression of $E_{F,h}(\tau)$ is derived in Appendix C in terms of the wave momentum flux $T(\xi,\tau)$ and wave momentum density $p(\xi,\tau)$ [26] and reads

$$E_{F,h}(\tau) = v\left(T_0^+ - vp_0^+\right) - v\left(T_0^- - vp_0^-\right). \tag{31}$$

The expressions for T and p are also derived in Appendix C. While Eqs. (30)–(31) are *exact* even in the presence of guideway damping, to be able to unambiguously distinguish between normal and anomalous Doppler waves, the damping in the guideway is assumed to be absent (i.e., $c_d = 0$). In this limit case, harmonic purely *propagating* waves can exist for which the following relations between the time-averaged wave energy and wave momentum hold true [26]:

$$\overline{h}_i = v_i^p \overline{p}_i, \qquad \overline{S}_i = v_i^p \overline{T}_i, \tag{32}$$

where subscript i represents the wave index and v_i^p is the phase velocity of the ith harmonic propagating wave. Substituting Eqs. (30)–(32) into the guideway contribution $\overline{E}_{gw}$ to the mass energy variation (Eq. (29)), we obtain

$$\overline{E}_{gw} = \sum_{i=1}^{4}\left(\frac{v}{v_i^p} - 1\right)\overline{W}_i, \tag{33}$$

$$\overline{W}_i = +\left(\overline{S}_{0,i}^+ - v\overline{h}_{0,i}^+\right), \qquad i = 1,4, \tag{34}$$

$$\overline{W}_i = -\left(\overline{S}_{0,i}^- - v\overline{h}_{0,i}^-\right), \qquad i = 2,3, \tag{35}$$

where $\overline{W}$ represents the averaged energy dissipated by the wave radiation in the guideway, $i = 1,4$ represent the two harmonic waves in front of the vehicle while $i = 2,3$ represent the two harmonic waves behind the vehicle. For example, to compute $\overline{S}_{0,1}^+$, the wave corresponding to $e^{-ik_1\xi}$ from Eq. (A.12) is substituted in Eq. (B.13), then evaluated at $\xi = 0$, and finally averaged over one oscillation period. It must be emphasized that the number of waves depends on the type of guideway and this number applies to the beam on elastic foundation considered in this study.

Making use of the relation $\frac{v}{v_i^p} - 1 = -\frac{\Omega}{\omega_i}$ (stemming from the kinematic invariant relation for a moving harmonic force intersecting with the dispersion curve, see [26] Eq. (5)), Eq. (33) can now be re-written as

$$\overline{E}_{gw} = \underbrace{\Omega\sum_{i=1}^{2}\frac{\overline{W}_i^{anom}}{|\omega_i|}}_{\overline{E}_{gw}^{anom}} - \underbrace{\Omega\sum_{i=3}^{4}\frac{\overline{W}_i^{norm}}{|\omega_i|}}_{\overline{E}_{gw}^{norm}}, \tag{36}$$

where ω_i is the frequency of the ith harmonic wave, superscripts anom and norm stand for anomalous and normal Doppler waves, respectively, and $i = 1, 2$ are anomalous Doppler waves while $i = 3, 4$ are normal Doppler waves. Normal Doppler waves have either a negative phase velocity ($v^{\mathrm{p}} < 0$) or phase velocity larger than the vehicle velocity ($v^{\mathrm{p}} > v$), while anomalous Doppler waves have a phase velocity smaller than the vehicle velocity ($v^{\mathrm{p}} < v$) [26].

Eq. (36) clearly shows that, since the $\overline{W}_i$ is positive definite, the anomalous Doppler waves contribute positively to $\overline{E}_{\mathrm{gw}}$ and consequently add energy to the mass energy variation $\overline{E}_{\mathrm{M}}$ while the normal ones dissipate energy (negative sign in Eq. (36)). Mathematically it appears that, for this type of guideway, the addition of energy by the anomalous Doppler waves stems from the negative value of their frequency ω_i. The mass energy variation (Eq. (28)) where the guideway contribution $\overline{E}_{\mathrm{gw}}$ is separated into normal and anomalous Doppler energy reads

$$\Delta E_{\mathrm{M}} = \overline{E}_{\mathrm{em}} + \overline{E}_{\mathrm{gw}}^{\mathrm{anom}} - \overline{E}_{\mathrm{gw}}^{\mathrm{norm}}. \tag{37}$$

It must be emphasized once more that this relation is exact only if $\overline{E}_{\mathrm{gw}}^{\mathrm{anom}}$ and $\overline{E}_{\mathrm{gw}}^{\mathrm{norm}}$ contain purely propagating waves (evanescent waves do not carry energy). Nonetheless, for a small amount of damping in the guideway Eq. (37), although not exact, can still be useful in determining the approximate contributions of each wave type to the stability of the system. Since the accurate determination of eigenvalues in Sections 5 and 6 requires a small amount of damping, the energy balance given by Eq. (37) is presented in the following for a system with a small amount of damping. However, for all results presented, we ensure that the *exact* $\overline{E}_{\mathrm{gw}}$ computed from Eq. (29) and the *approximate* $\overline{E}_{\mathrm{gw}}$ computed using Eq. (36) have a relative difference below 0.1%.

Fig. 12 presents the stable/unstable domains obtained using the *exact* $\overline{E}_{\mathrm{gw}}$ and the *approximate* $\overline{E}_{\mathrm{gw}}$. The almost perfect match demonstrates that the approximation introduced by Eq. (37) is minimal, and that the separation between the anomalous and normal Doppler waves is trust-worthy for the amount of damping used here.

Fig. 12 also presents the separate contributions to $\overline{E}_{\mathrm{M}}$ where $\overline{E}_{\mathrm{gw}}$ is split into the energy input by the anomalous $\overline{E}_{\mathrm{gw}}^{\mathrm{anom}}$ and normal $\overline{E}_{\mathrm{gw}}^{\mathrm{norm}}$ Doppler waves. For sub-critical velocities, the anomalous Doppler waves are not excited and, consequently, the same observations apply as for Fig. 10 where $\overline{E}_{\mathrm{gw}} = \overline{E}_{\mathrm{gw}}^{\mathrm{norm}}$. However, at super-critical velocities, the anomalous Doppler waves can be excited (depending on the vibration frequency Ω). The bottom panels of Fig. 12 prove that at $v = 1.3c_{\mathrm{cr}}$ the anomalous Doppler waves are very energetic and are the source of instability for the majority of the K_{p}–K_{d} parameter space, except for very small values of K_{d} where $\overline{E}_{\mathrm{em}}$ governs (which also causes instability). Fig. 12 proves that the drastic reduction of the stable domain observed above $v = 1.3c_{\mathrm{cr}}$ is caused by the anomalous Doppler waves.

To conclude this section, we emphasize the need for a shift in the conventional control design strategy. Typically, control systems are designed to maximize energy dissipation, ensuring rapid decay of perturbations. In the current system, that would correspond to increasing the K_{d} value. However, as shown in Figs. 7 and 8, increasing K_{d} at super-critical velocities can have negative effects. As discussed in Sections 7.1 and 7.2, altering K_{d} changes the frequency of free vibrations induced by perturbations, potentially triggering the wave-induced instability mechanism. In other words, while increasing K_{d} enhances energy dissipation, it may also activate wave-induced instability, destabilizing the system. An improved control design strategy should balance both objectives: maximizing energy dissipation while avoiding the activation of wave-induced instability (specifically by steering clear of problematic free-vibration frequency ranges). The results and methodology presented in this work can guide the development of more effective control strategies.

8. Conclusions

From a practical standpoint, this study examined the stability of a magnetically suspended moving vehicle (e.g., Maglev or Hyperloop) and its dependence on both vehicle velocity and control gains. From a theoretical perspective, the paper explored the interaction between two distinct instability mechanisms present in such systems: (i) instability induced by improper control of the electromagnetic suspension, and (ii) wave-induced instability. To facilitate this analysis, the infinite guideway was properly accounted for, allowing the vehicle velocity to affect system stability. This approach differs from those in existing literature, where the guideway is either assumed to be rigid or modeled as a single-degree-of-freedom system. The novelty of this work lies not only in its theoretical contribution but also in its practical implications for designing the control strategy and/or the guideway.

The results indicate that for sub-critical velocities, the frequency and vehicle-velocity dependent reaction force from the guideway can help suppress perturbations and expand the stable parameter space. At these velocities, any instability is solely due to the improper control of the electromagnetic suspension, as wave-induced instability cannot occur at sub-critical speeds. However, at certain super-critical velocities, the stable parameter space shrinks significantly, a consequence of the activation of the wave-induced instability mechanism and its interaction with the electromagnetic instability. Additionally, near the stability boundaries, the system exhibits limit cycle oscillations (i.e., stability loss occurs through a supercritical Hopf-like bifurcation), but as control gains increase further, the limit cycles disappear.

To effectively mitigate instability, it is crucial to identify the dominant instability mechanism for a given set of control parameters. This study introduces a methodology that separates the contributions of each mechanism to the overall system stability by dividing the vehicle's energy variation into two components: (i) energy input from the electromagnetic suspension and (ii) energy input from the guideway. The results indicate that, beyond a certain super-critical velocity, wave-induced instability is activated across most of the control-gain plane, with the control strategy able to counteract this effect only in limited regions. Additionally, the study demonstrates that the physical source of the wave-induced instability in this system is the generation of anomalous Doppler waves that feed back their energy into the vehicle vibration.

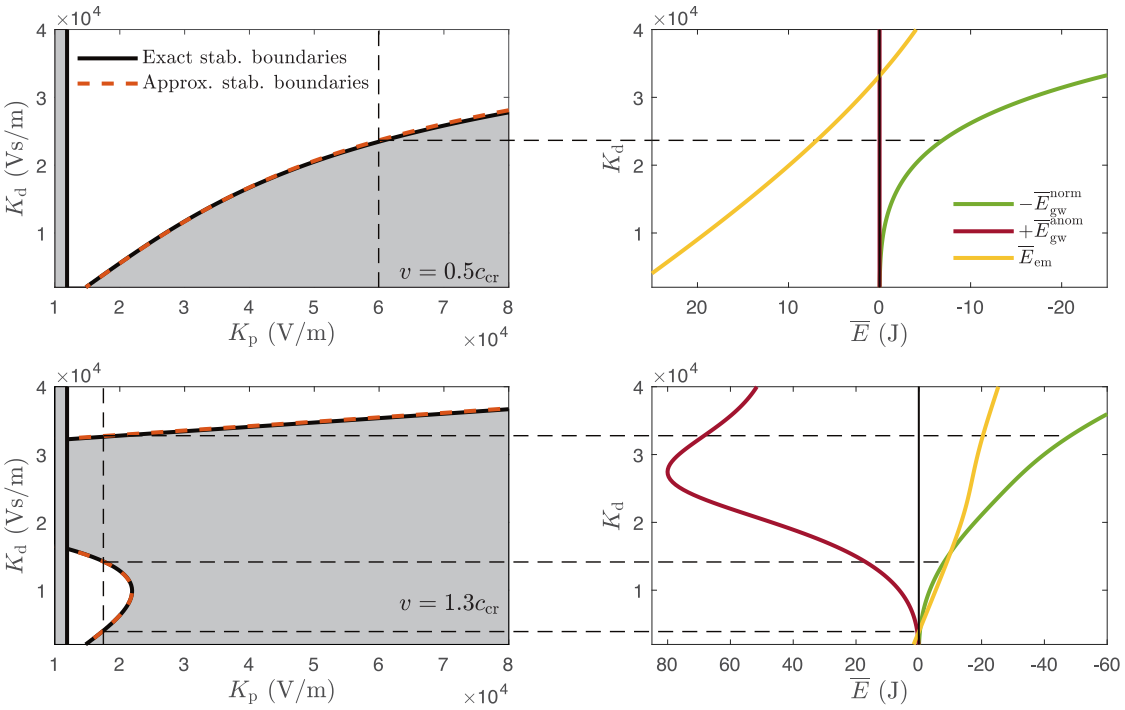

Fig. 12. Left panels: Stable/unstable domains in the K_p–K_d parameter space obtained using the *exact* $\overline{E}_{gw}$ and the *approximate* $\overline{E}_{gw}$. Right panels: energy input by the electromagnetic force $\overline{E}_{em}$, and by the anomalous $\overline{E}_{gw}^{anom}$ and normal $\overline{E}_{gw}^{norm}$ Doppler waves vs K_d for one value of K_p indicated by the vertical dashed black line in the left panels. These results are presented for two vehicle velocities: $v = 0.5c_{cr}$ (top panels) and $v = 1.3c_{cr}$ (bottom panels). (For interpretation of the colors in this figure, the reader is referred to the online version of this article.).

In conclusion, this study highlights the need for a change in the conventional control design strategy. The typical approach, which focuses on maximizing energy dissipation through control, can trigger wave-induced instability in magnetically suspended moving vehicles interacting with guideways, leading to system destabilization. A more effective control design should balance two key goals: maximizing energy dissipation while preventing the activation of wave-induced instability, particularly by avoiding problematic free-vibration frequency ranges. The findings and methodology introduced in this work provide valuable insights for developing more robust control strategies.

CRediT authorship contribution statement

Andrei B. Fărăgău: Writing – original draft, Visualization, Validation, Software, Methodology, Investigation, Formal analysis, Conceptualization. **Andrei V. Metrikine:** Writing – review & editing, Supervision, Investigation. **Jithu Paul:** Writing – review & editing, Investigation. **Rens van Leijden:** Writing – review & editing, Investigation. **Karel N. van Dalen:** Writing – review & editing, Supervision, Investigation, Conceptualization.

Declaration of competing interest

The authors declare that they have no known competing financial interests or personal relationships that could have appeared to influence the work reported in this paper.

Acknowledgments

The authors express sincere gratitude to the European Union's Horizon Europe programme for its support through the Marie Skłodowska-Curie grant agreement No 101106482 (HySpeed project).

Appendix A. Response of the linearized system with imposed harmonic motion of the mass

To determine the mechanism that causes instability, Section 7 analyzes the variation of the vehicle energy at the stability boundaries. The stabilizing and destabilizing mechanisms balance out at the stability boundary, and, consequently, the system's response to a small perturbation is harmonic. In order to identify the stabilizing and destabilizing mechanisms, a harmonic motion

is imposed to the moving mass, and the resulting energy inputs by (i) the guideway and (ii) electromagnetic suspension are derived in Section 7. This appendix focuses solely on the derivation of the guideway response to a moving mass with imposed harmonic motion, which is used to compute the energy quantities in Section 7.

The linearized system described by Eqs. (19)–(22) is considered here as its response is utilized in the energy analysis (Section 7). Note that only the first equilibrium is of interest since the second one is unconditionally unstable; consequently, the linearization around the first equilibrium is considered in this section. The expressions presented in this section are simplified compared to Eqs. (19)–(22) by making use of the fact that $\Delta_{\mathrm{ss,1}} = \Delta_{\mathrm{targ}}$; consequently, some terms from Eqs. (19)–(22) drop.

Firstly, the equation of motion for the mass (Eq. (20)) is eliminated because the mass motion is no longer a degree of freedom but is instead imposed as a harmonic motion with frequency Ω and amplitude A_0. The displacement of the mass is given by

$$u(\tau) = A_0 \cos(\Omega\tau). \tag{A.1}$$

Next, because the response of the guideway at the left and right of the contact point is required (see Section 7), the Eq. (1) (but with F_{tr} instead of F) is used instead of the integro-differential equation given in Eq. (19). The system of equations for the scenario considered here reads (the subscript tr is omitted for brevity)

$$EI\frac{\partial^4 w}{\partial\xi^4} + \rho\left(\frac{\partial^2 w}{\partial\tau^2} - 2v\frac{\partial^2 w}{\partial\xi\partial\tau} + v^2\frac{\partial^2 w}{\partial\xi^2}\right) + c_{\mathrm{d}}\left(\frac{\partial w}{\partial\tau} - v\frac{\partial w}{\partial\xi}\right) + k_{\mathrm{d}} w = -F(\tau)\delta(\xi), \tag{A.2}$$

$$F(\tau) = \frac{2CI_{\mathrm{ss}}^2}{\Delta_{\mathrm{ss}}^3}\left(\frac{\Delta_{\mathrm{ss}}}{I_{\mathrm{ss}}} I + A_0\cos(\Omega\tau) - w_0\right), \tag{A.3}$$

$$\frac{\mathrm{d}I}{\mathrm{d}\tau} = \frac{\Delta_{\mathrm{ss}}}{2C}\left[-IR + K_{\mathrm{p}}\left(w_0 - A_0\cos(\Omega\tau)\right) + \left(K_{\mathrm{d}} + \frac{2CI_{\mathrm{ss}}}{\Delta_{\mathrm{ss}}^2}\right)\left(\frac{\mathrm{d}w_0}{\mathrm{d}\tau} + A_0\Omega\sin(\Omega\tau)\right)\right], \tag{A.4}$$

The steady-state response is sought for, so the response is assumed as follows:

$$w(\xi,\tau) = \mathrm{Re}\left(W(\xi)\mathrm{e}^{\mathrm{i}\Omega\tau}\right), \qquad I(\tau) = \mathrm{Re}\left(I_0\mathrm{e}^{\mathrm{i}\Omega\tau}\right). \tag{A.5}$$

These expressions are first substituted into Eq. (A.4) and the complex current amplitude I_0 is expressed in terms of the mass and beam displacement amplitudes:

$$I_0 = \frac{\frac{\Delta_{\mathrm{ss}}}{2C}\left(K_{\mathrm{p}} + \mathrm{i}\Omega K_{\mathrm{d}}\right) + \mathrm{i}\Omega\frac{I_{\mathrm{ss}}}{\Delta_{\mathrm{ss}}}}{\mathrm{i}\Omega + \frac{\Delta_{\mathrm{ss}}R}{2C}}\left[W_0 - A_0\right], \tag{A.6}$$

where $W_0 = W(\xi = 0)$. Eq. (A.2) can now be re-written as

$$EI\frac{\mathrm{d}^4 W}{\mathrm{d}\xi^4} + \rho\left(-\Omega^2 W - 2v\mathrm{i}\Omega\frac{\mathrm{d}W}{\mathrm{d}\xi} + v^2\frac{\mathrm{d}^2 W}{\mathrm{d}\xi^2}\right) + c_{\mathrm{d}}\left(\mathrm{i}\Omega W - v\frac{\mathrm{d}W}{\mathrm{d}\xi}\right) + k_{\mathrm{d}} W = -F_0(W_0, A_0)\delta(\xi), \tag{A.7}$$

$$F_0(W_0, A_0) = \frac{2CI_{\mathrm{ss}}^2}{\Delta_{\mathrm{ss}}^3}\left(1 - \frac{\Delta_{\mathrm{ss}}}{I_{\mathrm{ss}}}\frac{\frac{\Delta_{\mathrm{ss}}}{2C}\left(K_{\mathrm{p}} + \mathrm{i}\Omega K_{\mathrm{d}}\right) + \mathrm{i}\Omega\frac{I_{\mathrm{ss}}}{\Delta_{\mathrm{ss}}}}{\mathrm{i}\Omega + \frac{\Delta_{\mathrm{ss}}R}{2C}}\right)\left(A_0 - W_0\right), \tag{A.8}$$

where $F_0(W_0, A_0)$ is obtained from Eq. (A.3) when Eqs. (A.5) and (A.6) are substituted. The only remaining unknown is W, and it can be obtained by splitting Eq. (A.7) into two domains, one for $\xi < 0$ and one for $\xi > 0$ (similar to the procedure in [51]). This leads to two homogeneous ordinary differential equations since the concentrated force is moved to the interface conditions between the two domains, which read

$$W_{\mathrm{l}} = W_{\mathrm{r}}, \qquad \frac{\mathrm{d}W_{\mathrm{l}}}{\mathrm{d}\xi} = \frac{\mathrm{d}W_{\mathrm{r}}}{\mathrm{d}\xi}, \qquad \frac{\mathrm{d}^2 W_{\mathrm{l}}}{\mathrm{d}\xi^2} = \frac{\mathrm{d}^2 W_{\mathrm{r}}}{\mathrm{d}\xi^2}, \qquad -\frac{\mathrm{d}^3 W_{\mathrm{l}}}{\mathrm{d}\xi^3} + \frac{\mathrm{d}^3 W_{\mathrm{r}}}{\mathrm{d}\xi^3} = -\frac{F_0(W_0, A_0)}{EI}, \qquad \xi = 0, \tag{A.9}$$

with subscripts l and r representing the left ($\xi < 0$) and right ($\xi > 0$) domains, respectively. The responses $W_{\mathrm{l,r}}$ of the two homogeneous ordinary differential equations can be sought for in the form of harmonic functions:

$$W_{\mathrm{l,r}}(\xi) = C_{\mathrm{l,r}}\mathrm{e}^{-\mathrm{i}k\xi}, \tag{A.10}$$

where k is the wavenumber determined from the characteristic equation which is obtained after substitution of Eq. (A.10) into any one of the two homogeneous partial differential equations (i.e., Eq. (A.7) with zero right-hand side). The amplitudes $C_{\mathrm{l,r}}$ are obtained after applying the conditions at infinity and the interface conditions Eqs. (A.9). Their expressions and those of the wavenumbers k_{1-4} are not given here for brevity, but can be obtained straightforwardly using a symbolic mathematical software (e.g., Maple or Mathematica). The final expressions for w_{l} and w_{r} are

$$w_{\mathrm{l}}(\xi,\tau) = \mathrm{Re}\left[\left(C_{\mathrm{l},2}\mathrm{e}^{-\mathrm{i}k_2\xi} + C_{\mathrm{l},3}\mathrm{e}^{-\mathrm{i}k_3\xi}\right)\mathrm{e}^{\mathrm{i}\Omega\tau}\right], \qquad \xi \le 0, \tag{A.11}$$

$$w_{\mathrm{r}}(\xi,\tau) = \mathrm{Re}\left[\left(C_{\mathrm{r},1}\mathrm{e}^{-\mathrm{i}k_1\xi} + C_{\mathrm{l},4}\mathrm{e}^{-\mathrm{i}k_4\xi}\right)\mathrm{e}^{\mathrm{i}\Omega\tau}\right], \qquad \xi \ge 0. \tag{A.12}$$

The expression for the guideway velocity under the vehicle necessary in Section 7.1 to compute the energy input by the guideway reads

$$\frac{\mathrm{d}w_0}{\mathrm{d}\tau} = \frac{\mathrm{d}}{\mathrm{d}\tau}w_{\mathrm{l}}(\xi = 0, \tau) = \mathrm{Re}\left[\mathrm{i}\Omega\left(C_{\mathrm{l},2} + C_{\mathrm{l},3}\right)\mathrm{e}^{\mathrm{i}\Omega\tau}\right] \tag{A.13}$$

$$= \frac{\mathrm{d}}{\mathrm{d}\tau} w_{\mathrm{r}}(\xi = 0, \tau) = \mathrm{Re}\left[\mathrm{i}\Omega \left(C_{\mathrm{r},1} + C_{\mathrm{l},4}\right) \mathrm{e}^{\mathrm{i}\Omega\tau}\right]. \tag{A.14}$$

Since the velocity is continuous at $\xi = 0$, $\frac{\mathrm{d}w_0}{\mathrm{d}\tau}$ can be computed using either $w_{\mathrm{l}}(\xi = 0, \tau)$ or $w_{\mathrm{r}}(\xi = 0, \tau)$.

For the expressions required to determine the fluxes and densities in Section 7.2 and Appendix B, Eq. (A.11) is used for the expressions evaluated at $\xi = 0^-$ while Eq. (A.12) is used for the expressions evaluated at $\xi = 0^+$.

Appendix B. The guideway contribution to the mass energy variation

This appendix derives the expression for the guideway contribution to the mass energy variation used in Section 7. We start with the equation of motion of the guideway in the stationary reference frame (note that the subscript tr is omitted for brevity):

$$EI\frac{\partial^4 w}{\partial x^4} + \rho\frac{\partial^2 w}{\partial t^2} + c_{\mathrm{d}}\frac{\partial w}{\partial t} + k_{\mathrm{d}} w = -F(t)\delta(x - vt). \tag{B.1}$$

Note that the partial derivatives $\frac{\partial}{\partial x}$ and $\frac{\partial}{\partial t}$ are in the stationary reference frame.

To obtain equations describing energy variation in time, the equation of motion (that represents balance of vertical forces) is multiplied by the velocity $\frac{\partial w}{\partial t}$. We perform the following mathematical manipulations

$$EI\frac{\partial^4 w}{\partial x^4}\frac{\partial w}{\partial t} = EI\frac{\partial}{\partial x}\left(\frac{\partial^3 w}{\partial x^3}\frac{\partial w}{\partial t} - \frac{\partial^2 w}{\partial x^2}\frac{\partial^2 w}{\partial x \partial t}\right) + \frac{\partial}{\partial t}\left[\frac{1}{2}EI\left(\frac{\partial^2 w}{\partial x^2}\right)^2\right], \tag{B.2}$$

$$\rho\frac{\partial^2 w}{\partial t^2}\frac{\partial w}{\partial t} = \frac{\partial}{\partial t}\left[\frac{1}{2}\rho\left(\frac{\partial w}{\partial t}\right)^2\right], \qquad k_{\mathrm{d}} w\frac{\partial w}{\partial t} = \frac{\partial}{\partial t}\left(\frac{1}{2}k_{\mathrm{d}} w^2\right). \tag{B.3}$$

The resulting equation describing the energy variation over time and space reads

$$\frac{\partial}{\partial x}S(x,t) + \frac{\partial}{\partial t}h(x,t) + c_{\mathrm{d}}\left(\frac{\partial w}{\partial t}\right)^2 = -F(t)\frac{\partial w}{\partial t}\delta(x - vt), \tag{B.4}$$

$$S(x,t) = EI\left(\frac{\partial^3 w}{\partial x^3}\frac{\partial w}{\partial t} - \frac{\partial^2 w}{\partial x^2}\frac{\partial^2 w}{\partial x \partial t}\right), \qquad h(x,t) = \frac{1}{2}EI\left(\frac{\partial^2 w}{\partial x^2}\right)^2 + \frac{1}{2}\rho\left(\frac{\partial w}{\partial t}\right)^2 + \frac{1}{2}k_{\mathrm{d}} w^2, \tag{B.5}$$

where $S(x,t)$ and $h(x,t)$ represent energy flux and elastic energy density, respectively.

We are interested in the energy variation in the immediate vicinity of the moving vehicle (E_{gw} is proportional to $\frac{\mathrm{d}w_0}{\mathrm{d}\tau}$), so we integrate the whole energy balance, Eq. (B.4), over a very small domain moving together with the vehicle (i.e., $x \in [vt - \epsilon, vt + \epsilon]$ where ϵ is a small spatial quantity). The spatial integral of the flux term can be taken directly while for the elastic energy density and damping terms, it requires some manipulation. To this end, we take the time derivative of the elastic energy density out of the spatial integral, and because the integration limits are time dependent, the Leibniz integration rule is required. The expression thus becomes

$$\int_{x=vt-\epsilon}^{x=vt+\epsilon}\left\{\frac{\partial}{\partial t}h + c_{\mathrm{d}}\left(\frac{\partial w}{\partial t}\right)^2\right\}\mathrm{d}x = \frac{\partial}{\partial t}\int_{x=vt-\epsilon}^{x=vt+\epsilon} h\mathrm{d}x - vh\Big|_{x=vt-\epsilon}^{x=vt+\epsilon} + \int_{x=vt-\epsilon}^{x=vt+\epsilon} c_{\mathrm{d}}\left(\frac{\partial w}{\partial t}\right)^2 \mathrm{d}x. \tag{B.6}$$

When we take the limit of ϵ going to zero, the integrals (first and last terms) in Eq. (B.6) tend to zero since none of the quantities inside has a delta-Dirac function (i.e., no energy is stored or dissipated in an infinitesimal domain). Consequently, the spatial integral of Eq. (B.4) becomes

$$\Big(S(x,t) - vh(x,t)\Big)\Big|_{x=vt+0} - \Big(S(x,t) - vh(x,t)\Big)\Big|_{x=vt-0} = -\int_{x=vt-0}^{x=vt+0} F(t)\frac{\partial w}{\partial t}\delta(x - vt)\mathrm{d}x. \tag{B.7}$$

In Eq. (B.7), S corresponds to the power flux through the cross-sections moving together with the vehicle, vh is an advective quantity representing the power density entering and exiting the infinitesimal area moving with the vehicle, and the right-hand side represents the power input by the vehicle.

Taking advantage of the Dirac delta function, the right-hand side becomes

$$-\int_{x=vt-0}^{x=vt+0} F(t)\frac{\partial w}{\partial t}\delta(x - vt)\mathrm{d}x = -F(t)\frac{\partial w}{\partial t}\Big|_{x=vt}. \tag{B.8}$$

It must be emphasized that the term $\frac{\partial w}{\partial t}\Big|_{x=vt}$ is obtained by first taking the partial derivative with respect to time and then evaluating it at $x = vt$, which is not the same quantity as $\frac{\mathrm{d}w_0}{\mathrm{d}\tau}$. Since the mass energy variation given by Eq. (27) is expressed in terms of $\frac{\mathrm{d}w_0}{\mathrm{d}\tau}$, Eq. (B.8) is re-written in the following. To this end, we perform a variable change from $\{x,t\}$ to $\{\xi = x - vt, \tau = t\}$. The partial derivatives in the new coordinate system become $\frac{\partial}{\partial t} = \frac{\partial}{\partial \tau} - v\frac{\partial}{\partial \xi}$ and $\frac{\partial}{\partial x} = \frac{\partial}{\partial \xi}$. Consequently, the partial time derivative of $w(x,t)$ transformed to the new coordinate system becomes

$$\frac{\partial}{\partial t}w(x,t) = \frac{\partial}{\partial \tau}w(\xi,\tau) - v\frac{\partial}{\partial \xi}w(\xi,\tau). \tag{B.9}$$

In the above expression, evaluating the left-hand side at $x = vt$ is equivalent with evaluating the right-hand side at $\xi = 0$, thus obtaining

$$\frac{\partial w(x,t)}{\partial t}\Big|_{x=vt} = \frac{\partial}{\partial \tau}w(\xi = 0, \tau) - v\frac{\partial w(\xi,\tau)}{\partial \xi}\Big|_{\xi=0}. \tag{B.10}$$

Since $w(\xi = 0, \tau) = w_0$, the final expression becomes

$$\frac{\partial w(x,t)}{\partial t}\Big|_{x=vt} = \frac{\mathrm{d}w_0}{\mathrm{d}\tau} - v\frac{\partial w}{\partial \xi}\Big|_{\xi=0}. \tag{B.11}$$

Eq. (B.11) is now substituted in Eq. (B.7) leading to the following expression (note that the left-hand side of Eq. (B.7) is also transformed to the moving reference frame for consistency)

$$-\left(S_0^+ - vh_0^+\right) + \left(S_0^- - vh_0^-\right) = -F(\tau)\frac{\mathrm{d}w_0}{\mathrm{d}\tau} + vF(\tau)\frac{\partial w}{\partial \xi}\Big|_{\xi=0}, \tag{B.12}$$

where $S_0^+ = S(\xi = 0^+, \tau)$ and $h_0^+ = h(\xi = 0^+, \tau)$ are quantities evaluated just in front of the moving mass and $S_0^- = S(\xi = 0^-, \tau)$ and $h_0^- = h(\xi = 0^-, \tau)$ are quantities evaluated just behind the moving mass. The quantities S and h are transformed to the moving-reference frame from Eq. (B.5) by using $\frac{\partial}{\partial t} = \frac{\partial}{\partial \tau} - v\frac{\partial}{\partial \xi}$ and $\frac{\partial}{\partial x} = \frac{\partial}{\partial \xi}$ and the chain-rule for higher-order derivatives. Their expressions read

$$S(\xi, \tau) = EI\left[\frac{\partial^3 w}{\partial \xi^3}\left(\frac{\partial w}{\partial \tau} - v\frac{\partial w}{\partial \xi}\right) - \frac{\partial^2 w}{\partial \xi^2}\left(\frac{\partial^2 w}{\partial \xi \partial \tau} - v\frac{\partial^2 w}{\partial \xi^2}\right)\right], \tag{B.13}$$

$$h(\xi, \tau) = \frac{1}{2}\left[EI\left(\frac{\partial^2 w}{\partial \xi^2}\right)^2 + \rho\left(\frac{\partial w}{\partial \tau} - v\frac{\partial w}{\partial \xi}\right)^2 + k_\mathrm{d} w^2\right]. \tag{B.14}$$

For the expressions evaluated at $\xi = 0^-$, we apply Eq. (A.11), while for those evaluated at $\xi = 0^+$, we use Eq. (A.12).

Eq. (B.12) is re-written to obtain the final expression for the energy variation of an infinitesimal domain of the guideway moving together with the vehicle, and reads

$$F(\tau)\frac{\mathrm{d}w_0}{\mathrm{d}\tau} = \left(S_0^+ - vh_0^+\right) - \left(S_0^- - vh_0^-\right) + E_{\mathrm{F,h}}(\tau), \qquad E_{\mathrm{F,h}} = vF(\tau)\frac{\partial w}{\partial \xi}\Big|_{\xi=0}. \tag{B.15}$$

Eq. (B.15) is equivalent to Eq. (30) used in Section 7.2.

Eq. (B.15) expresses that the energy input $E_\mathrm{gw} = F(\tau)\frac{\mathrm{d}w_0}{\mathrm{d}\tau}$ by the guideway (see Eq. (27)) is composed of the energy input $E_\mathrm{F,h}$ by the horizontal force required to maintain the constant velocity of the vehicle (see also [51,54] for an in-depth derivation and analysis of this force) from which the energy flowing in and out of the moving infinitesimal domain is subtracted.

Appendix C. Energy input by the horizontal force in terms of wave-momentum flux and density

Section 7.2 derives the individual energy contributions of the normal and anomalous Doppler waves to the vehicle's energy variation. It does this by expressing the energy input $E_\mathrm{F,h}$, provided by the horizontal force that sustains the vehicle's motion, in terms of the wave momentum flux T and momentum density p (refer to Eq. (31)). Although Eq. (31) is directly introduced in Section 7.2, this appendix details the derivation of the given expression. Note that another expression for $E_\mathrm{F,h}$ has already been introduced by Eq. (B.15) and derived in Appendix A; however, to separate the contributions of the normal and anomalous Doppler waves, the expression derived in this appendix is required.

In the absence of external forces, the variation of the moving mass (vehicle) longitudinal momentum P_0 reads [26]

$$\frac{\mathrm{d}P_0}{\mathrm{d}t} = -\Big[T(x,t) - vp(x,t)\Big]_{x=vt+0} + \Big[T(x,t) - vp(x,t)\Big]_{x=vt-0} + F_\mathrm{h}(t), \tag{C.1}$$

where F_h is the force maintaining the horizontal movement. In the present case of constant forward velocity (i.e., $x = vt$ where v is constant), the momentum P_0 is constant in time [26]. Consequently, the horizontal force becomes

$$F_\mathrm{h}(t) = \Big[T(x,t) - vp(x,t)\Big]_{x=vt+0} - \Big[T(x,t) - vp(x,t)\Big]_{x=vt-0}. \tag{C.2}$$

The energy input $E_\mathrm{F,h}$ is obtained through multiplying Eq. (C.2) by the horizontal velocity v, thus obtaining

$$E_\mathrm{F,h}(t) = v\Big[T(x,t) - vp(x,t)\Big]_{x=vt+0} - v\Big[T(x,t) - vp(x,t)\Big]_{x=vt-0}. \tag{C.3}$$

Eq. (C.3) is now transformed to the moving-reference frame leading to the following expressions:

$$E_\mathrm{F,h}(\tau) = v\left(T_0^+ - vp_0^+\right) - v\left(T_0^- - vp_0^-\right), \tag{C.4}$$

where $T_0^+ = T(\xi = 0^+, \tau)$, $p_0^+ = p(\xi = 0^+, \tau)$, $T_0^- = T(\xi = 0^-, \tau)$ and $p_0^- = p(\xi = 0^-, \tau)$.

As mentioned at the beginning of this appendix, there are two equivalent expressions for $E_\mathrm{F,h}$: Eq. (B.15) (used in Section 7.1 and derived in Appendix B), and Eq. (C.4) (presented in Section 7.2, namely Eq. (31)). The said expressions are time averaged over one oscillation period $\Theta = \frac{2\pi}{\Omega}$, and read

$$\overline{E}^\mathrm{A}_\mathrm{F,h} = v\frac{1}{\Theta}\int_0^\Theta F(\tau)\frac{\partial w}{\partial \xi}\Big|_{\xi=0}\mathrm{d}\tau, \tag{C.5}$$

$$\overline{E}^\mathrm{B}_\mathrm{F,h} = v\left(\overline{T}_0^+ - v\overline{p}_0^+\right) - v\left(\overline{T}_0^- - v\overline{p}_0^-\right), \tag{C.6}$$

where the overbar indicates that the quantity has been averaged over one period, $F(\tau)$ is the (vertical) electromagnetic force, and $\frac{\partial w}{\partial \xi}\Big|_{\xi=0}$ is the guideway slope evaluated at the position of the vehicle.

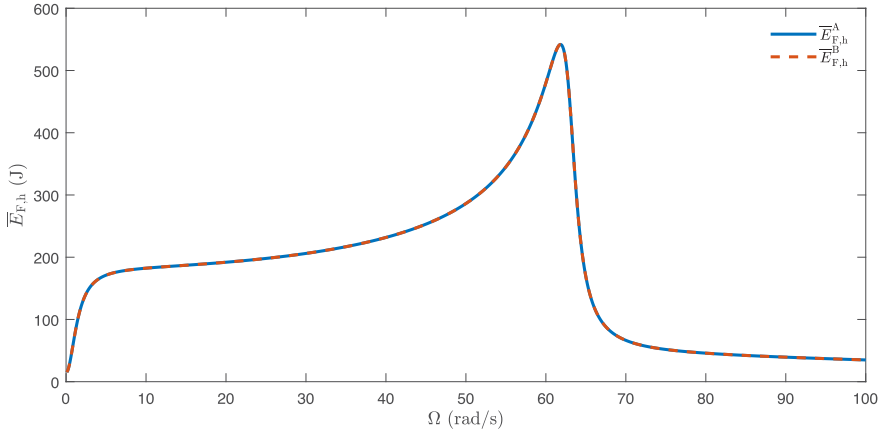

Fig. C.13. Comparison of the two expression for the averaged energy input $\overline{E}_{\mathrm{F,h}}$ by the horizontal force maintaining the constant mass velocity; $v = 1.3c_{\mathrm{cr}}$, $K_{\mathrm{p}} = 20$ (kV/m), and $K_{\mathrm{d}} = 20$ (kVs/m). The same excellent match is found for other system parameters. (For interpretation of the colors in this figure, the reader is referred to the online version of this article.).

To demonstrate that the two expressions are equivalent, we derive the expressions for T and p and compare the two expressions for multiple frequencies of vibration Ω. The expressions for T and p in the stationary-reference frame read [26]

$$T(x,t) = \frac{1}{2}\rho\left(\frac{\partial w}{\partial t}\right)^2 + \frac{1}{2}EI\left(\frac{\partial^2 w}{\partial x^2}\right)^2 - EI\frac{\partial w}{\partial x}\frac{\partial^3 w}{\partial x^3} - \frac{1}{2}k_{\mathrm{d}}w^2, \tag{C.7}$$

$$p(x,t) = -\rho\frac{\partial w}{\partial x}\frac{\partial w}{\partial t}. \tag{C.8}$$

Eqs. (C.7)–(C.8) are transformed to the moving-reference frame by using $\frac{\partial}{\partial t} = \frac{\partial}{\partial \tau} - v\frac{\partial}{\partial \xi}$ and $\frac{\partial}{\partial x} = \frac{\partial}{\partial \xi}$ and the chain-rule for higher-order derivatives, and their expressions read

$$T(\xi,\tau) = \frac{1}{2}\rho\left(\frac{\partial w}{\partial \tau} - v\frac{\partial w}{\partial \xi}\right)^2 + \frac{1}{2}EI\left(\frac{\partial^2 w}{\partial \xi^2}\right)^2 - EI\frac{\partial w}{\partial \xi}\frac{\partial^3 w}{\partial \xi^3} - \frac{1}{2}k_{\mathrm{d}}w^2, \tag{C.9}$$

$$p(\xi,\tau) = -\rho\frac{\partial w}{\partial \xi}\left(\frac{\partial w}{\partial \tau} - v\frac{\partial w}{\partial \xi}\right). \tag{C.10}$$

Using the expressions from Appendix A in which a harmonic motion is imposed to the mass, all the necessary derivatives of w can be computed analytically (their expressions are not given here for brevity).

Fig. C.13 presents the averaged energy input by the horizontal force obtained with the two expressions (Eqs. (C.5) and (C.6)) for varying Ω and one K_{p}–K_{d} pair. The excellent match proves that the two expressions are equivalent. The same excellent match is found for other system parameters, but these are not presented here for brevity.

Data availability

No data was used for the research described in the article.

References

[1] D. Stăncioiu, H. Ouyang, J.E. Mottershead, Vibration of a beam excited by a moving oscillator considering separation and reattachment, J. Sound Vib. 310 (4–5) (2008) 1128–1140, http://dx.doi.org/10.1016/j.jsv.2007.08.019.

[2] T. Mazilu, Instability of a train of oscillators moving along a beam on a viscoelastic foundation, J. Sound Vib. 332 (19) (2013) 4597–4619, http://dx.doi.org/10.1016/j.jsv.2013.03.022.

[3] N.A. Alexander, M.M. Kashani, Exploring bridge dynamics for ultra-high-speed, hyperloop, trains, Structures 14 (2018) 69–74, http://dx.doi.org/10.1016/j.istruc.2018.02.006.

[4] E. Ahmadi, N.A. Alexander, M.M. Kashani, Lateral dynamic bridge deck-pier interaction for ultra-high-speed Hyperloop train loading, Proc. Inst. Civ. Eng.: Bridg. Eng. 173 (3) (2020) 198–206, http://dx.doi.org/10.1680/jbren.19.00011.

[5] T. Lu, S. Yuan, T. Wang, X. Liu, P. Wang, R. Chen, Dynamic response and wave motion of a periodically supported beam under an ultra-high-speed load: Wave dispersion and critical velocities, Int. J. Solids Struct. 291 (2024) 112694, http://dx.doi.org/10.1016/j.ijsolstr.2024.112694.

[6] Y. Shan, B. Albers, S.A. Savidis, Influence of different transition zones on the dynamic response of track-subgrade systems, Comput. Geotech. 48 (2013) 21–28, http://dx.doi.org/10.1016/j.compgeo.2012.09.006.

[7] J.N. Varandas, P. Hölscher, M.A. Silva, Settlement of ballasted track under traffic loading: Application to transition zones, Proc. Inst. Mech. Eng. Part F J. Rail Rapid Transit 228 (3) (2014) 242–259, http://dx.doi.org/10.1177/0954409712471610.

[8] J.C. Nielsen, X. Li, Railway track geometry degradation due to differential settlement of ballast/subgrade – Numerical prediction by an iterative procedure, J. Sound Vib. 412 (2018) 441–456, http://dx.doi.org/10.1016/j.jsv.2017.10.005.

[9] J.M. de Oliveira Barbosa, A.B. Fărăgău, K.N. van Dalen, M. Steenbergen, Modelling ballast via a non-linear lattice to assess its compaction behaviour at railway transition zones, J. Sound Vib. 530 (2022) 116942, http://dx.doi.org/10.1016/j.jsv.2022.116942.

[10] A.B. Fărăgău, J.M. de Oliveira Barbosa, A.V. Metrikine, K.N. van Dalen, Dynamic amplification in a periodic structure with a transition zone subject to a moving load: three different phenomena, Math. Mech. Solids 27 (9) (2022) 1740–1760, http://dx.doi.org/10.1177/10812865221094318.

[11] A.V. Metrikine, Parametric instability of a moving particle on a periodically supported infinitely long string, J. Appl. Mech. Trans. ASME 75 (1) (2008) 0110061–0110068, http://dx.doi.org/10.1115/1.2745368.

[12] S.N. Verichev, A.V. Metrikine, Instability of vibrations of a mass that moves uniformly along a beam on a periodically inhomogeneous foundation, J. Sound Vib. 260 (5) (2003) 901–925, http://dx.doi.org/10.1016/S0022-460X(02)00936-7.

[13] K. Abe, Y. Chida, P.E. Balde Quinay, K. Koro, Dynamic instability of a wheel moving on a discretely supported infinite rail, J. Sound Vib. 333 (15) (2014) 3413–3427, http://dx.doi.org/10.1016/j.jsv.2014.03.027.

[14] K. Gkoumas, Hyperloop academic research: A systematic review and a taxonomy of issues, Appl. Sci. Switz. 11 (13) (2021) http://dx.doi.org/10.3390/app11135951.

[15] P. Museros, C. Lázaro, B. Pinazo, S. Monleón, Key aspects in the analysis and design of Hyperloop™ infrastructure under static, dynamic and thermal loads, Eng. Struct. 239 (April) (2021) http://dx.doi.org/10.1016/j.engstruct.2021.112177.

[16] Y. Cai, S.S. Chen, D.M. Rote, H.T. Coffey, Vehicle/guideway dynamic interaction in Maglev systems, J. Dyn. Syst. Meas. Control. Trans. ASME 118 (3) (1996) 526–530, http://dx.doi.org/10.1115/1.2801176.

[17] J. Hu, W. Ma, X. Chen, S. Luo, Levitation stability and hopf bifurcation of EMS Maglev trains, Math. Probl. Eng. 2020 (2020) http://dx.doi.org/10.1155/2020/2936838.

[18] J. Paul, K.N. van Dalen, A.B. Fărăgău, R.J. van Leijden, M. Ouggaâli, A.V. Metrikine, Suppressing parametric resonance of a hyperloop vehicle using a parametric force, Phys. Rev. E 111 (2025) 034210, http://dx.doi.org/10.1103/PhysRevE.111.034210.

[19] Y. Cai, S.S. Chen, Numerical analysis for dynamic instability of electrodynamic Maglev systems, Shock. Vib. 2 (4) (1995) 339–349, http://dx.doi.org/10.3233/SAV-1995-2407.

[20] D.M. Rote, Y. Cai, Review of dynamic stability of repulsive-force Maglev suspension systems, IEEE Trans. Magn. 38 (2 II) (2002) 1383–1390, http://dx.doi.org/10.1109/20.996030.

[21] A.S. Abdelrahman, J. Sayeed, M.Z. Youssef, Hyperloop transportation system: Analysis, design, control, and implementation, IEEE Trans. Ind. Electron. 65 (9) (2018) 7427–7436, http://dx.doi.org/10.1109/TIE.2017.2777412.

[22] W.Q. Zhang, J. Li, K. Zhang, P. Cui, Stability and bifurcation in magnetic flux feedback Maglev control system, Math. Probl. Eng. 2013 (2013) http://dx.doi.org/10.1155/2013/537359.

[23] H. Wu, X.H. Zeng, D.G. Gao, J. Lai, Dynamic stability of an electromagnetic suspension Maglev vehicle under steady aerodynamic load, Appl. Math. Model. 97 (2021) 483–500, http://dx.doi.org/10.1016/j.apm.2021.04.008.

[24] H. Yabuno, T. Seino, M. Yoshizawa, Y. Tsujioka, Dynamical behaviour of a levitated body with magnetic guides, JSME Int. J. 32 (3) (1989) 428–435.

[25] G.G. Denisov, E.K. Kugusheva, V.V. Novikov, On the problem of the stability of one-dimensional unbounded elastic systems, J. Appl. Math. Mech. 49 (4) (1985) 533–537, http://dx.doi.org/10.1016/0021-8928(85)90065-6.

[26] M. A.V., Unstable vertical oscillations of an object moving uniformly along an elastic guide as a result of an anomalous Doppler effect, Acoust. Phys. 40 (1) (1994) 85–89.

[27] A.V. Metrikine, H.A. Dieterman, Instability of vibrations of a mass moving uniformly along an axially compressed beam on a viscoelastic foundation, J. Sound Vib. 201 (5) (1997) 567–576, http://dx.doi.org/10.1006/jsvi.1996.0783.

[28] T. Mazilu, M. Dumitriu, C. Tudorache, Instability of an oscillator moving along a Timoshenko beam on viscoelastic foundation, Nonlinear Dynam. 67 (2) (2012) 1273–1293, http://dx.doi.org/10.1007/s11071-011-0068-5.

[29] V. Stojanović, M.D. Petković, J. Deng, Stability of vibrations of a moving railway vehicle along an infinite complex three-part viscoelastic beam/foundation system, Int. J. Mech. Sci. 136 (2018) 155–168, http://dx.doi.org/10.1016/j.ijmecsci.2017.12.024.

[30] C. Rodrigues, F.M.F. Simões, A. Pinto da Costa, D. Froio, E. Rizzi, Finite element dynamic analysis of beams on nonlinear elastic foundations under a moving oscillator, Eur. J. Mech. A Solids 68 (2018) 9–24, http://dx.doi.org/10.1016/j.euromechsol.2017.10.005.

[31] Z. Dimitrovová, On the critical velocity of moving force and instability of moving mass in layered railway track models by semi-analytical approaches, Vibration 6 (1) (2023) 113–146, http://dx.doi.org/10.3390/vibration6010009.

[32] Z. Dimitrovová, Instability of vibrations of mass(es) moving uniformly on a two-layer track model: Parameters leading to irregular cases and associated implications for railway design, Appl. Sci. Switz. 13 (22) (2023) http://dx.doi.org/10.3390/app132212356.

[33] Y. Cai, S.S. Chen, T.M. Mulcahy, Dynamic Stability of Maglev Systems, Tech. Rep., Argonne National Laboratory, 1992.

[34] J.D. Yau, Vibration control of Maglev vehicles traveling over a flexible guideway, J. Sound Vib. 321 (1–2) (2009) 184–200, http://dx.doi.org/10.1016/j.jsv.2008.09.030.

[35] Z. Sun, Moving-inertial-loads-induced dynamic instability for slender beams considering parametric resonances, J. Vib. Acoust. 138 (1) (2016) 1–9, http://dx.doi.org/10.1115/1.4031518.

[36] R. Bogacz, S. Nowakowski, K. Popp, On the stability of a Timoshenko beam on an elastic foundation under a moving spring-mass system, Acta Mech. 61 (1986) 117–127, http://dx.doi.org/10.1007/BF01184842.

[37] A.V. Metrikine, K. Popp, Instability of vibrations of an oscillator moving along a beam on an elastic half-space, Eur. J. Mech. A Solids 18 (2) (1999) 331–349, http://dx.doi.org/10.1016/S0997-7538(99)80020-5.

[38] S.N. Veritchev, Instability of a Vehicle Moving on an Elastic Structure (Ph.D. thesis), Delft University of Technology, 2002.

[39] R. Galluzzi, S. Circosta, N. Amati, A. Tonoli, A. Bonfitto, T.A. Lembke, M. Kertész, A multi-domain approach to the stabilization of electrodynamic levitation systems, J. Vib. Acoust. Trans. the ASME 142 (6) (2020) 1–30, http://dx.doi.org/10.1115/1.4046952.

[40] J. Xu, C. Chen, D. Gao, S. Luo, Q. Qian, Nonlinear dynamic analysis on Maglev train system with flexible guideway and double time-delay feedback control, J. Vibroeng. 19 (8) (2017) 6346–6362, http://dx.doi.org/10.21595/jve.2017.18970.

[41] J.S. Lee, S.D. Kwon, M.Y. Kim, I.H. Yeo, A parametric study on the dynamics of urban transit Maglev vehicle running on flexible guideway bridges, J. Sound Vib. 328 (3) (2009) 301–317, http://dx.doi.org/10.1016/j.jsv.2009.08.010.

[42] E. Kong, J.S. Song, B.B. Kang, S. Na, Dynamic response and robust control of coupled Maglev vehicle and guideway system, J. Sound Vib. 330 (25) (2011) 6237–6253, http://dx.doi.org/10.1016/j.jsv.2011.05.031.

[43] X.J. Zheng, J.J. Wu, Y.H. Zhou, Numerical analyses on dynamic control of five-degree-of-freedom Maglev vehicle moving on flexible guideways, J. Sound Vib. 235 (1) (2000) 43–61, http://dx.doi.org/10.1006/jsvi.1999.2911.

[44] X.J. Zheng, J.J. Wu, Y.H. Zhou, Effect of spring non-linearity on dynamic stability of a controlled Maglev vehicle and its guideway system, J. Sound Vib. 279 (1–2) (2005) 201–215, http://dx.doi.org/10.1016/j.jsv.2003.10.025.

[45] C.F. Zhao, W.M. Zhai, Maglev vehicle/guideway vertical random response and ride quality, Veh. Syst. Dyn. 38 (3) (2002) 185–210, http://dx.doi.org/10.1076/vesd.38.3.185.8289.

[46] A.B. Fărăgău, R. Wang, A.V. Metrikine, K.N. Van Dalen, The interplay between the electro-magnetic and wave-induced instability mechanisms in the Hyperloop transportation system, in: Advances in Nonlinear Dynamics, ICNDA 2023, in: NODYCON Conference Proceedings Series, vol. I, 2023.

[47] A.B. Fărăgău, A.V. Metrikine, K.N. van Dalen, Transition radiation in a piecewise-linear and infinite one-dimensional structure–a Laplace transform method, Nonlinear Dynam. 98 (2019) 2435–2461, http://dx.doi.org/10.1007/s11071-019-05083-6.
[48] A.B. Fărăgău, T. Mazilu, A.V. Metrikine, T. Lu, K.N. van Dalen, Transition radiation in an infinite one-dimensional structure interacting with a moving oscillator—The Green's function method, J. Sound Vib. 492 (2021) 115804, http://dx.doi.org/10.1016/j.jsv.2020.115804.
[49] J.M. de Oliveira Barbosa, A.B. Fărăgău, K.N. van Dalen, A lattice model for transition zones in ballasted railway tracks, J. Sound Vib. 494 (2021) 115840, http://dx.doi.org/10.1016/j.jsv.2020.115840.
[50] A.B. Fărăgău, C. Keijdener, J.M. de Oliveira Barbosa, A.V. Metrikine, K.N. van Dalen, Transition radiation in a nonlinear and infinite one-dimensional structure: a comparison of solution methods, Nonlinear Dynam. 103 (2021) 1365–1391.
[51] A.B. Fărăgău, Understanding Degradation Mechanisms at Railway Transition Zones Using Phenomenological Models (Ph.D. thesis), Delft University of Technology, 2023.
[52] A.R.M. Wolfert, Wave Effects in One-Dimensional Elastic Systems Interacting with Moving Loads (Ph.D. thesis), Delft University of Technology, 1999.
[53] J.S. Chen, S.Y. Chen, W.Z. Hsu, Effects of geometric nonlinearity on the response of a long beam on viscoelastic foundation to a moving mass, J. Sound Vib. 497 (2021) http://dx.doi.org/10.1016/j.jsv.2021.115961.
[54] A.I. Vesnitskii, A.V. Metrikin, Transition radiation in mechanics, Phys.-Uspekhi 39 (10) (1996) 983–1007.